

The mesosphere and thermosphere of Titan revealed by Cassini/UVIS stellar occultations

T.T. Koskinen^{a,*}, R.V. Yelle^a, D.S. Snowden^a, P. Lavvas^a, B.R. Sandel^a, F.J. Capalbo^b, Y. Benilan^b, R.A. West^c

^a Lunar and Planetary Laboratory, University of Arizona, 1629 E. University Blvd., Tucson, AZ 85721, USA

^b Laboratoire Interuniversitaire des Systèmes Atmosphériques (LISA), Universités Paris, Est Creteil et Paris Diderot, 61 Avenue du Général de Gaulle, 94010 Créteil Cedex, France

^c Jet Propulsion Laboratory, California Institute of Technology, Pasadena, CA 91109, USA

ARTICLE INFO

Article history:

Received 7 June 2011

Revised 21 September 2011

Accepted 22 September 2011

Available online 10 October 2011

Keywords:

Titan

Occultations

Atmospheres, Structure

ABSTRACT

Stellar occultations observed by the Cassini/UVIS instrument provide unique data that probe the mesosphere and thermosphere of Titan at altitudes between 400 and 1400 km. This region is a site of complex photochemistry that forms hydrocarbon and nitrile species, and plays a crucial role in the formation of the organic hazes observed in the stratosphere, but has yet to be adequately characterized. We analyzed publicly available data obtained between flybys Tb in December 2004 and T58 in July 2009, with an emphasis on two stable occultations obtained during flybys T41 and T53. We derived detailed density profiles for CH₄, C₂H₂, C₂H₄, C₄H₂, HCN, HC₃N and C₆H₆ between ~400 and 1200 km and extinction coefficients for aerosols between 400 and 900 km. Our analysis reveals the presence of extinction layers in the occultation data that are associated with large perturbations in the density profiles of the gaseous species and extinction profiles of the aerosols. These relatively stable features vary in appearance with location and change slowly over time. In particular, we identify a sharp extinction layer between 450 and 550 km that coincides with the detached haze layer. In line with recent images obtained by Cassini/ISS, the altitude of this layer changes rapidly around the equinox in 2009. Our results point to unexpected complexity that may have significant consequences for the dynamics and physical processes taking place in the upper atmosphere of Titan.

© 2011 Elsevier Inc. All rights reserved.

1. Introduction

Cassini/UVIS stellar occultations probe Titan's atmosphere between the altitudes of 400–1400 km. This altitude range includes the 'agnostosphere' from 500 to 950 km that is poorly characterized because it falls between the thermosphere that is probed directly by the Cassini Ion and Neutral Mass Spectrometer (INMS) (e.g., Waite et al., 2005) and Cassini Plasma Spectrometer (CAPS) (e.g., Coates et al., 2007), and the stratosphere that is probed primarily by observations of thermal infrared emissions (e.g., Coustenis et al., 2010; Vinatier et al., 2010a). Solar Lyman α radiation is mostly absorbed in the agnostosphere near 800 km. Because Lyman α radiation is a primary driver of neutral photochemistry, the agnostosphere is a critical region for the production of many hydrocarbon and nitrile species that are observed in the stratosphere and on the surface of Titan. It is also the transition region between the thermosphere, where solar EUV radiation drives high energy ion chemistry that forms many complex molecules (e.g.,

Vuitton et al., 2009), and the stratosphere, which is dominated by organic hazes. The formation of the haze depends on seed particles that are generated by photochemistry. Detailed analysis of the density profiles of minor species in the agnostosphere is therefore important to understanding the composition of the atmosphere as a whole. It can also reveal clues as to how aerosols grow from small seed particles into large fractal aggregates observed in the main haze layer in the stratosphere (Tomasko et al., 2008).

Apart from stellar occultations, the only comprehensive measurements of the agnostosphere are the temperature and density profiles obtained by the Huygens Atmospheric Structure Instrument (HASI) (Fulchignoni et al., 2005) and the density profiles of CH₄, C₂H₂, and C₂H₄ derived from solar occultations observed by the Voyager Ultraviolet Spectrometer (UVS) (Broadfoot et al., 1981; Smith et al., 1982; Vervack et al., 2004). HCN and HC₃N were also detected in the UVS data but the low spectral resolution did not allow for the density profiles to be derived for these species (Vervack et al., 2004). More recently, the composition of the agnostosphere has also been constrained by analysis of airglow spectra observed with the Cassini Ultraviolet Imaging Spectrograph (UVIS) (Ajello et al., 2007, 2008; Stevens et al., 2011).

* Corresponding author. Fax: +1 520 621 4933.

E-mail address: tommi@lpl.arizona.edu (T.T. Koskinen).

The occultations of α Virginis and λ Scorpii that took place in December 2004 during flyby Tb offered the first view into the mesosphere and lower thermosphere on Titan (Shemansky et al., 2005; Liang et al., 2007). The analysis of these occultations by Shemansky et al. (2005) revealed the presence of CH₄, C₂H₂, C₂H₄, C₂H₆, C₄H₂ and HCN in the data whereas Liang et al. (2007) used the Tb data to detect and characterize aerosols at altitudes between 500 and 1000 km. The detection of aerosols in this region implies that they are formed at high altitudes in the thermosphere. These results represent a significant advance in the characterization of Titan's upper atmosphere; however, neither Shemansky et al. (2005) or Liang et al. (2007) presented detailed number density profiles for the minor species identified in the data and their analysis did not include all of the species that are detectable.

Here, we reanalyze the Tb occultations and also present the first analyses of several other stellar occultations that took place between December 2004 and April 2009. In addition to the species already identified by Shemansky et al. (2005), we derive density profiles for HC₃N and C₆H₆. Ferradaz et al. (2009) argued earlier that HC₃N would be detectable in the UVIS data with a sufficiently high signal to noise (S/N) and we confirm that this is the case. The detection of C₆H₆ is important because it may play a significant role in forming the seed particles for aerosol growth (Lavvas et al., 2011). We also confirm the presence of aerosols and show that extinction due to aerosols increases with decreasing altitude below 700 km. We determine the altitude of the detached haze layer (Porco et al., 2005) from the occultation data as a function of time and show that the results are consistent with recent images of the layer obtained by the Cassini Imaging Science Subsystem (ISS) (West et al., 2011).

We present detailed density profiles for all of the minor species identified in the data and extinction profiles for the aerosols. The profiles were derived from two occultations observed during flyby T41 in February 2008 and T53 in April 2009. These occultations were chosen because of the pointing stability of the spacecraft during the measurements and a high altitude resolution of 0.4–2 km. These data allow for a significantly higher signal to noise (S/N) than that obtained for the Tb occultations. The density profiles were retrieved between ~600 and 1200 km for CH₄, between ~400 and 1000 km for C₂H₂, C₂H₄ and C₄H₂, between ~500 and 1000 km for HCN and HC₃N, and between ~400 and 900 km for C₆H₆. The extinction coefficients for the aerosols were derived for altitudes between 400 and 900 km. In general, the number density profiles have an altitude resolution of 10–50 km, depending on the quality of the retrieval for each species.

The light curves¹ derived from several occultations reveal evidence for distinct extinction layers in the data. We show that these layers are associated with large perturbations in the density profiles of the minor species and the extinction coefficients of the aerosols. In particular, we identify two distinct layers: a low altitude layer between 450 and 550 km and a high altitude layer, which appears either as a broad extinction layer centered around 600 km or as a sharp layer between 700 and 800 km. The low altitude layer coincides with the detached haze layer (Porco et al., 2005) whereas the high altitude layer arises mostly from perturbations in the density profiles of the gaseous species. We note that similar layers were observed before in the Voyager/UVS light curves near 385 km and between 630 and 770 km (Broadfoot et al., 1981; Smith et al., 1982).

The temperature profiles derived from the data also contain perturbations with characteristics similar to those seen in the HASI data (Fulchignoni et al., 2005). These perturbations have a vertical wavelength of 100–200 km and an amplitude of 10–20 K. Strobel

(2006) suggested that such perturbations are gravitational tidal waves. We show that the large perturbations in the density profiles of the minor species are also consistent with slowly varying waves such as those driven by the tides – although other possibilities exist and our findings should be confirmed by future studies and new observations.

The layout of the paper is as follows: Section 2 covers the observations and data reduction. It includes details on the initial data reduction, the quality and stability of the observations and analysis of the transmission spectra and density profiles. It also includes details of the data simulation and analysis of synthetic occultations. In Section 3 we discuss the appearance of the extinction layers and compare the altitude of the detached haze layer with ISS measurements. By careful analysis of the transmission spectra, we show how different absorbers are identified and discuss the density profiles of the gaseous absorbers. We also derive the extinction profiles for the aerosols and constrain their properties by using the data. In Section 4 we discuss the variability in the temperature profiles and calculate chemical and transport timescales to analyze the density profiles of the minor species. In Section 4, we also briefly address the evolution of the aerosols as they move to lower altitudes from the production region. The summary of our results and concluding remarks are included in Section 5.

2. Methods

2.1. Observations and data reduction

The occultations were observed by the FUV channel (1120–1910 Å) of the UVIS instrument (McClintock et al., 1993; Esposito et al., 2004). The instrument consists of a telescope, a toroidal grating spectrograph, and a two-dimensional pulse counting micro-channel plate detector equipped with a Coded Anode Array Converter (CODACON) readout anode. The size of the telescope entrance pupil is 20 × 20 mm, the telescope is equipped with an off-axis parabolic mirror with dimensions of 22 × 33 mm and a focal length of 100 mm. The CODACON array consists of 1024 × 64 (spectral × spatial) 'pixels', each with dimensions of 0.025 × 0.1 mm and a width of 0.78 Å in the spectral dimension. The FUV channel has three changeable slits with widths of 0.075 mm (high resolution), 0.15 mm (low resolution), and 0.8 mm (occultation slit). All of the occultations we analyzed were observed with the low resolution slit, which has a field of view (FOV) of 1.5 × 60 mrad.

We obtained the occultation data from the archive of the Planetary Data System (PDS). Details on the timing of the observations and observing geometry are included in Table 1 for several flybys. For each occultation, we calculated transmission as a function of impact parameter a and wavelength bin denoted by the central wavelength λ_p . In general, the image of the star was recorded on a limited section of the detector array that varied in spatial width between 5 and 9 pixels. Due to the point spread function (PSF) of the instrument, most of the signal is contained within one central pixel of the image with only a small fraction of the counts in the surrounding pixels. In order to obtain a single spectrum for each impact parameter, we summed the signal over the spatial pixels within each wavelength bin without accounting for possible sub-pixel variations of the detector PSF. Often the detector background signal can be estimated from dark images obtained during the occultation while the line of sight (LOS) to the star is optically thick. The dark count in the UVIS images appears sporadically as random single count peaks, implying that the dark current of the detector is barely registered as 1 analogue-to-digital unit (ADU). These random peaks cannot be analyzed statistically and consequently we made no attempt to remove the dark current from the data.

¹ A light curve refers to transmission as a function of impact parameter. Impact parameter refers to the shortest distance between the line of sight from the UVIS instrument to the occulted star and the surface of Titan.

Table 1
Stellar occultations.

Flyby ^a	Date	Star	(LAT,LON) ^b	Local time (h)	Type	Z _D (km) ^c
Tb I	12/13/2004	α Vir	(58,315)	1.53	2	N/A
Tb II	12/13/2004	λ Sco	(−36,318)	1.33	1	510
T21	12/12/2006	α Eri	(−36,118)	6.03	1	510
T23	01/13/2007	η UMa	(−5,232)	22.5	1	510
T41 I	02/23/2008	ϵ CMa	(−6,333)	2.42	1	498
T41 II	02/23/2008	ϵ CMa	(−27,175)	13.3	1	498
T47 I	11/19/2008	η UMa	(1,24)	20.7	2	500
T47 II	11/19/2008	β CMa	(56,340)	23.7	N/A	N/A
T48	12/05/2008	ϵ CMa	(19,320)	0.97	2	520
T52	04/03/2009	α Eri	(37,313)	12.9	2	450
T53	04/19/2009	α Eri	(39,296)	14.0	2	450
T58	07/08/2009	η UMa	(−11,31)	7.55	2	450

^a Note that the list of occultations is not complete. We excluded some occultations severely compromised by data drop outs.

^b The coordinates are given for the impact parameter of $a \approx 500$ km.

^c Altitude of the detached haze layer (corresponds to the center of the layer as determined from light curves).

As a result of this initial processing, we obtained the spectra of the occulted star, measured in detector counts, as a function of time for each occultation. In order to relate these spectra to altitudes in the atmosphere, we calculated the impact parameters by using the appropriate SPICE kernels and subroutines provided by the Navigation and Ancillary Information Facility (NAIF). In most cases the star was not observed at the center of the slit and the LOS to the star did not coincide with the instrument boresight vector; therefore we calculated the orientation of the LOS and the location of the star in the FOV of the instrument by using its right ascension (α) and declination (δ) from the Hipparcos catalogue. We updated these coordinates to the epoch of the observations by taking into account the proper motion of the star and used them to calculate the impact parameter and location of the nearpoint² on the surface of Titan as a function of time.

Based on the measured spectra, the observed transmission $T(a, \lambda_p)$ is given by:

$$T(a, \lambda_p) = \frac{S(a, \lambda_p)}{S_0(\lambda_p)} \quad (1)$$

where $S(a, \lambda_p)$ is the transmitted spectrum as a function of impact parameter, and $S_0(\lambda_p)$ is the reference spectrum of the star, both in detector counts. The latter is obtained by averaging $S(a, \lambda_p)$ over all impact parameters higher than a limit above which the atmosphere is transparent. We identified this limit by dividing the data into 100 Å bins between $\lambda_p = 1200$ –1900 Å and fitting an exponential function to the resulting light curves. The limit varies from 1200 to 1600 km and generally decreases with increasing wavelength due to the effect of different absorbers and their density profiles in the atmosphere. As a result, we assumed that the atmosphere is transparent at $a \geq 1650$ km and calculated $S_0(\lambda_p)$ accordingly. We used the T41 I and T53 occultations (Table 1) for detailed analysis of density and temperature profiles. In order to do so, we binned the data to altitude resolutions between 1 and 10 km. For both occultations, the resulting signal to noise (S/N) at the chosen altitude resolution is much better than that based on the Tb occultations with a vertical resolution of 25 km (Shemansky et al., 2005).

In order to explore the stability of the spacecraft during all of the occultations, we used the stellar coordinates to map the location of the star in the spectrograph slit as a function of time. This analysis revealed that the pointing was stable during T21, T41, and T53. However, during all of the other occultations the star

moved slightly in the FOV, occasionally even drifting in and out of the slit. For each occultation, we cross-correlated the transmission spectra $S(a, \lambda_p)$ obtained from $a > 1650$ km with the reference spectrum $S_0(\lambda_p)$. The results indicate that the pointing drift is associated with a wavelength shift. Also, in some cases the light curves show evidence for substantial flux variations, particularly when the star is drifting towards the edge of the slit. It may be possible to correct the data for some of the occultations by developing a calibration algorithm that correlates the wavelength shift and the flux variations with the position of the star in the slit. This is beyond the scope of the present work and at this point we chose to retrieve density profiles from stable occultations only.

The PDS archive files provide a separate calibration algorithm for each occultation that can be used to convert detector counts to “apparent” radiance and vice versa. Fig. 1 shows the calibrated reference spectrum of ϵ CMa obtained from the T41 I occultation, compared with a spectrum of the star obtained from the IUE archive. This comparison shows that the calibration algorithm performs satisfactorily and that the IUE spectrum can be used in the forward model for fitting transmission spectra and creating synthetic occultations for testing the retrieval (see Sections 2.2 and 2.3). There are some disagreements between the UVIS and IUE spectra at wavelengths between 1200 and 1350 Å and near 1550 Å but these do not affect our analysis. We note that the reported wavelength resolution of the low resolution slit is 4.8 Å (Esposito et al., 2004) but this only applies to extended sources. For point sources such as a star the wavelength resolution is determined by the line spread function (LSF) of the instrument. The LSF was measured for the H Ly α line (1215.67 Å) and can be approximated by a central Gaussian distribution with a standard deviation of ~ 1.2 Å and two Lorentzian distributions that capture the broad wings of the line profile (Greg Holsclaw, *personal communication*). The Gaussian component dominates and consequently we adopted a Gaussian LSF with a standard deviation of 1.2 Å for retrieval purposes.

The S/N of the UVIS instrument is described by (Esposito et al., 2004):

$$N^2(a, \lambda_p) = S(a, \lambda_p) + B\delta t \quad (2)$$

where B is the detector dark count per pixel per second and δt is the integration time. This implies that S/N is determined by photon counting statistics. We verified that this is the case by exploring

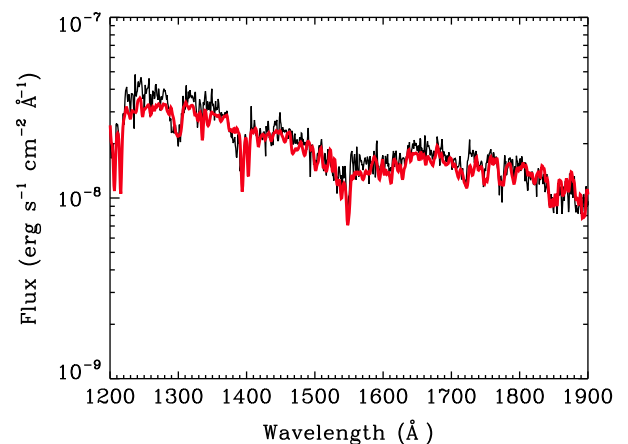


Fig. 1. The FUV spectrum of ϵ CMa from the IUE archive (thick red line) and based on calibrated UVIS observations (black line). The IUE spectrum was convolved to the resolution of the UVIS instrument and binned to UVIS spectral elements with a width of 0.78 Å. The figure shows that the calibration algorithm provided by the PDS performs satisfactorily. (For interpretation of the references to color in this figure legend, the reader is referred to the web version of this article.)

² Nearpoint refers to the point on the surface of Titan directly below the tangent point of the LOS on a circle with a radius given by the impact parameter a .

the UVIS spectra of ϵ CMA retrieved from $a \geq 1650$ km in different wavelength bins. Fig. 2 shows the signal as a function of impact parameter for a wavelength bin centered at $\lambda_p = 1500.46$ Å together with a histogram of the counts. We fitted Gaussian and Poisson distributions to similar histograms in different wavelength bins and generally obtained standard deviations that are in very good agreement with Eq. (2). The disagreement with Gaussian statistics is less than 10% for 96% of the pixels at wavelengths between 1200 and 1900 Å. We note that many of the ‘bad’ pixels are located at $\lambda_p > 1800$ Å, where the count rate is low. Based on this analysis, we calculated the uncertainty on the transmission curves based on the observed signal simply by using standard formulae of error propagation for normally distributed errors.

2.2. Retrieval of atmospheric properties

The observed transmission is related to the properties of the atmosphere by:

$$T(a, \lambda_p) = \frac{\int d\lambda' R(\lambda_p, \lambda') T_{atm}(a, \lambda') F_0(\lambda')}{\int d\lambda' R(\lambda_p, \lambda') F_0(\lambda')} \quad (3)$$

where $R(\lambda_p, \lambda)$ is the instrument response function, $T_{atm}(a, \lambda)$ is the atmospheric transmission function, and $F_0(\lambda)$ is the flux of the star. We note that airglow and light scattered into the FOV of the instrument by the atmosphere do not affect the observed transmission in

the wavelength range of the FUV channel significantly. We verified this by comparing the apparent radiance of the UVIS spectra with airglow measurements. The FUV airglow spectrum of Titan has been measured both off the disk (Ajello et al., 2008) and off the limb at altitudes above 750 km (Stevens et al., 2011). The spectrum consists of emissions from N_2 excited by photoelectron impact and solar UV light, resonantly scattered H Ly α radiation and sunlight reflected by N_2 and modified by aerosol and hydrocarbon absorption. At wavelengths between 1250 and 1900 Å the emission features in the limb spectra have a maximum radiance of ~ 3 $R\text{\AA}^{-1}$ whereas the disk emission increases with wavelength, reaching a radiance of ~ 30 $R\text{\AA}^{-1}$ at 1900 Å. The two stars of interest to the present study are ϵ CMA (T41) and α Eri (T53). The flux measured by UVIS for the fainter of the stars, ϵ CMA, varies between $\sim 10^{-9}$ and 10^{-8} $\text{erg s}^{-1} \text{cm}^{-2} \text{\AA}^{-1}$ (corresponding to ~ 1 – 20 $\text{kR}\text{\AA}^{-1}$ in calibrated UVIS data) at relevant wavelengths for impact parameters ranging between 500 and 1000 km. This means that for the most part airglow is buried within the uncertainty of the data. Further, the observed signal is not affected by refraction or scintillation by the atmosphere.

Given the above simplifications, the atmospheric transmission function is given by:

$$T_{atm}(a, \lambda) = \exp \left[- \sum_s \sigma_s^*(a, \lambda) N_s(a) \right] \quad (4)$$

where $N_s(a)$ is the column density of species s . The effective cross section (e.g., Kyroala et al., 2010) is defined as:

$$\sigma_s^*(a, \lambda) = \frac{2}{N_s(a)} \int_a^\infty \frac{\chi_s(r, \lambda) r dr}{\sqrt{r^2 - a^2}} \quad (5)$$

where r is the distance from the center of the planet and the local extinction coefficient is given by:

$$\chi_s(r, \lambda) = n_s(r) \sigma_s(r, \lambda) \quad (6)$$

where $n_s(r)$ is the local number density and $\sigma_s(r, \lambda)$ is the local extinction cross section. Generally, we assumed that the spectrum of the occulted star varies smoothly with wavelength and simplified Eq. (3) to:

$$T(a, \lambda_p) = \int d\lambda' R(\lambda_p, \lambda') T_{atm}(a, \lambda_p)$$

where $\int d\lambda' R(\lambda_p, \lambda') = 1$. We compared the results of the retrieval obtained with a forward model based on Eq. (3) and the archive spectra of the stars with the results obtained by using the simplified equation above and noted that the retrieved density profiles were not significantly different between the two cases.

Extinction in the mesosphere and lower thermosphere of Titan arises from absorption by hydrocarbon and nitrile species, and scattering and absorption by aerosols. We analyzed the transmission spectra at different impact parameters and used them to retrieve column densities based on the optical depth contributions of different species. In order to facilitate the retrieval of column densities, Eq. (3) can be written as:

$$\mathbf{T} = \mathbf{F}(\mathbf{N}) + \Delta\mathbf{T} \quad (7)$$

where \mathbf{F} is a forward model that relates the column densities \mathbf{N} of the different species to transmission \mathbf{T} measured at different wavelengths, and $\Delta\mathbf{T}$ represents the measurement errors. We solve this equation for \mathbf{N} by maximizing the conditional probability $P(\mathbf{N}|\mathbf{T})$ that, given values \mathbf{T} , the column densities are given by \mathbf{N} . This is equivalent to minimizing a cost function given by (e.g., Rodgers, 2000):

$$-2 \ln P(\mathbf{N}|\mathbf{T}) = [\mathbf{T} - \mathbf{F}(\mathbf{N})]^T \mathbf{S}_\epsilon^{-1} [\mathbf{T} - \mathbf{F}(\mathbf{N})] \quad (8)$$

where \mathbf{S}_ϵ^{-1} is a covariance matrix based on the measurement errors.

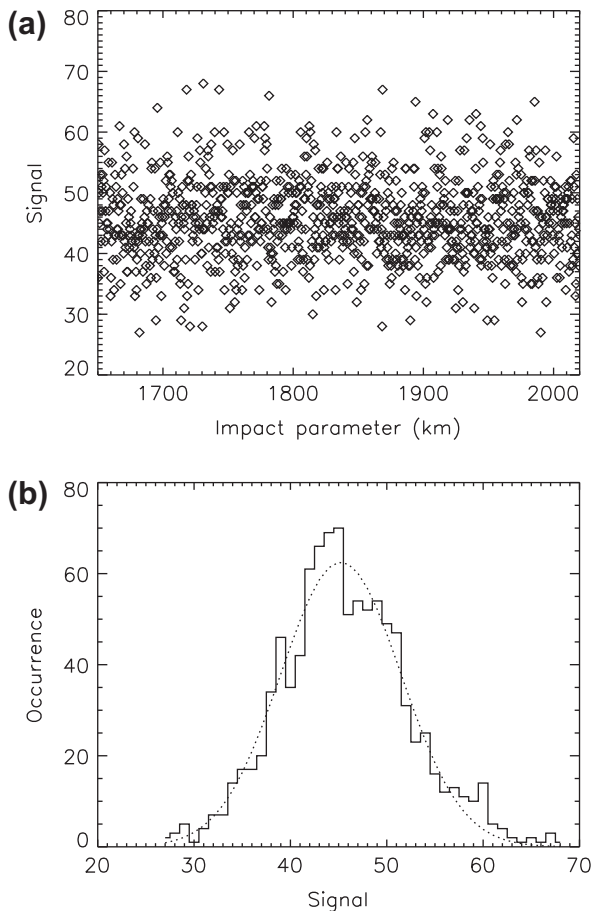


Fig. 2. (a) The observed signal from ϵ CMA as a function of impact parameter for a single pixel centered at $\lambda_p = 1500.46$ Å. The mean of the counts is 45.7 and the standard deviation implied by Eq. (2) is 6.7. (b) Histogram of the counts fitted by a Gaussian with a mean of 45.2 and a standard deviation of $\sigma = 6.2$. A Poisson distribution (not shown) fitted to the same data yields a mean of 45.9 and standard deviation of 6.8.

Several methods have been used to solve Eq. (7) in the past. In particular, Kyrola et al. (1993) studied the performance of methods that included variants of the Levenberg–Marquardt (LM) maximization of $P(\mathbf{N}|\mathbf{T})$, minimization of a linearized model, and various types of weighted least squares solutions. They found that a variant of the LM method that includes the instrument response function produces the best results and is also computationally the most effective. Consequently, we adopted the LM method for all of the column density retrievals. We note, however, that instead of convolving the cross sections with the instrument LSF separately, we convolved transmission in the forward model in line with Eq. (3).

As indicated by Eq. (3), the forward model is based on the response of the instrument, the properties of the atmosphere, and the extinction cross sections of different absorbers. We modeled instrument response by simulating line broadening based on the LSF discussed above. In addition to line broadening, instrument response may include effects such as flux variations caused by pointing drifts and internal scattering caused by instrument optics (e.g., Shemansky et al., 2005). As explained in Section 2.1, we mapped the location of star in the FOV during the occultations in order to check for pointing errors. Subsequently, we decided to limit the retrieval of density profiles to two of the stable occultations, namely T41 I and T53. Further, we assumed that internal scattering is limited to wavelengths near the H Ly α line and only analyzed data at wavelengths longer than 1250 Å. We did not find evidence for substantial corruption of the data in the T41 I or T53 occultations by internal scattering in this wavelength range.

In order to calculate atmospheric transmission, we used the most recent laboratory measurements of the absorption cross sections available for each species. The references and other information about the cross sections are included in Table 2. We note that the listed cross sections of HCN and C₆H₆ have not been used before in the analysis of UVIS data. For the most part, the measured cross sections apply to temperatures close to those in the upper atmosphere of Titan. The exceptions are HCN and C₆H₆ whose cross sections were measured close to or at room temperature (see Benilan, Y. et al., 2011, in preparation; Capalbo, F.J. et al., 2011, in preparation). We assumed that the cross sections do not change significantly with altitude, i.e., that they are not affected by temperature fluctuations in the atmosphere. This assumption is justified because the temperature fluctuations above $z = 500$ km in the atmosphere of Titan are of the order of ~ 10 – 20 K (e.g., Fulchignoni et al., 2005). These fluctuations are not large enough to affect the retrieval significantly (e.g., Capalbo, 2010) and, in any case, the cross sections were not measured at a sufficient sample of temperatures to justify complicating the analysis.

The extinction cross sections of the aerosols are uncertain. It is customary to assume that Titan aerosols are similar to laboratory tholins. In particular, the optical properties of Khare et al. (1984) tholins have been used extensively to characterize the extinction cross sections of the aerosols in previous studies. Recent modeling indicates that the size, shape and composition of the aerosols may change significantly below the lower edge of the primary production region near $z = 750$ km in Titan's mesosphere (Lavvas et al., 2010, 2011). Even if the aerosols are similar to the Khare et al. (1984) tholins in the stratosphere, this does not guarantee that the same is true in the thermosphere where the formation of the aerosols is initiated. With this caveat in mind, we nevertheless used the indices of refraction of the Khare et al. (1984) tholins to derive extinction cross sections for the aerosols from Mie theory. This is because at present there are few other constraints on the composition and optical properties of the high altitude aerosols. We also attempted to use the data to characterize the wavelength dependence of the extinction cross sections and compared the results with the Khare et al. (1984) tholins (see Section 3.4).

Having obtained the column density profiles, we converted them into local number density profiles. This is justified because for impact parameters below 1650 km the T41 I and T53 occultations span only a narrow range of latitudes and longitudes. In order to convert the column densities into number density profiles, we expressed the column density N_i at impact parameter a_i in discrete form as:

$$N_i = A_{ij}n_j + \Delta N_i \quad (9)$$

where ΔN_i is the error on N_i and the matrix A_{ij} is given by:

$$A_{ij} = 2 \int_{r_j}^{r_{j-1}} f(r) \frac{r dr}{\sqrt{r^2 - a_i^2}} \quad (10)$$

where $f(r)$ is some function that describes the variation of density with altitude within a single grid cell between r_{j-1} and r_j . We assumed that the density is constant within grid cells, i.e., that $f(r) = 1$.

The local density n_j at altitude z_j is obtained by inverting Eq. (9). However, a simple inversion leads to a magnification of the measurement errors that can corrupt the solution. In order to control the growth of the errors, we used the Tikhonov regularization technique (Tikhonov and Arsenin, 1977) to perform the inversion. This technique was previously used by Quemerai et al. (2006) in the analysis of Mars occultations and we closely followed their implementation of it. Thus the number densities are given by:

$$\mathbf{n} = (\mathbf{A}^T \mathbf{S}_\epsilon^{-1} \mathbf{A} + \phi_3 \mathbf{L}^T \mathbf{L})^{-1} \mathbf{A}^T \mathbf{S}_\epsilon^{-1} \mathbf{N} \quad (11)$$

Table 2
Absorption cross sections.

Species	Temperature (K)	Wavelengths (Å)	Resolution (Å)	References	Altitude range (km) ^a
CH ₄	150 R ^b	1250–1430 1430–1520	0.6 ~1	Chen and Wu (2004) Lee et al. (2001)	550–1300
C ₂ H ₂	150	1250–1900	0.07	Wu et al. (2001)	400–1200
C ₂ H ₄	140	1250–1900	0.6	Wu et al. (2004)	400–1200
C ₄ H ₂	173 R	1250–1700 1700–1950	0.5 ~1–6	Ferradaz et al. (2009) Fahr and Nayak (1994)	400–1000
C ₂ H ₆	150 R	1250–1500 1500–1600	0.6 ~1	Chen and Wu (2004) Lee et al. (2001)	400–700
C ₆ H ₆	R	1250–1900	1	Measured ^c	400–850
HCN	255	1250–1850	0.6	Measured	600–1000
HC ₃ N	203	1250–1900	0.5	Ferradaz et al. (2009)	500–1000
Tholins ^d	N/A	1250–1900	N/A	Khare et al. (1984)	400–900

^a Estimated range of impact parameters for reliable retrieval of column densities (see Section 2.3). Note that these limits may be different if the abundances of the absorbers differ significantly from those used in the data simulation.

^b Room temperature.

^c The cross sections of C₆H₆ and HCN were measured recently (Capalbo, F.J. et al., 2011, in preparation; Benilan, Y. et al., 2011, in preparation).

^d Calculated from Mie theory with the appropriate optical properties (see Section 3.4).

where ϕ_s is the regularization parameter and \mathbf{L} is a second derivative operator that smooths the solution in altitude. The matrix $\mathbf{G} = (\mathbf{A}^T \mathbf{S}_\epsilon^{-1} \mathbf{A} + \phi_s \mathbf{L}^T \mathbf{L})^{-1} \mathbf{A}^T \mathbf{S}_\epsilon^{-1}$ is known as the retrieval gain matrix and $\mathbf{G}\mathbf{A}$ is the averaging kernel matrix, which provides a diagnostic for the altitude resolution of the retrieval. We adopted a regularization parameter based on the measurement errors σ_a given by $\phi_s = \phi_0 / \sigma_a^2$ where ϕ_0 is an arbitrary constant. The inversion is iterative and proceeds until a satisfactory density profile is obtained. During each iteration, the altitude resolution is degraded while the errors get smaller. Based on the retrieved column densities of different species, we achieved vertical resolutions between 10 and 60 km for the number density profiles.

2.3. Data simulation

In order to test the reliability of the retrieval and to estimate the altitude ranges for which the density profiles of different species can safely be obtained, we created synthetic occultation data sets with different characteristics based on the orbital geometry of T41 I (Table 1). For the purposes of this simulation, we used a photochemical model to calculate realistic number density profiles for CH_4 , C_2H_2 , C_2H_4 , C_4H_2 , C_2H_6 , C_6H_6 , HCN and HC_3N (Lavvas et al., 2008a,b). These species are based on the absorbers that we identified in the data (see Section 3.2). The photochemical calculations assumed a solar activity and zenith angle appropriate to the time and latitude of the observations. We used the temperature profile measured by HASI (Fulchignoni et al., 2005) as input for the model. We converted the model number densities into LOS column abundances by using Eq. (10) with a vertical grid spacing of 0.1 km. We interpolated the column densities to the ~ 0.4 km resolution of the T41 I occultation and calculated the spectrum of optical depth for each impact parameter by using the absorption cross sections listed in Table 2. Instead of using the model to generate an extinction profile for the aerosols, we used an optical depth profile of the aerosols similar to the one retrieved from the data (see Section 3.4).

Based on the combined optical depth of all of the absorbers, we calculated atmospheric transmission as a function of impact parameter and wavelength. In order to simulate the observed signal from the occulted star, we used the IUE spectrum of ϵ CMa (Fig. 1). For each impact parameter, we multiplied the stellar flux by model transmission. Because the wavelength resolution of the high dispersion IUE spectrum is ~ 0.2 Å we degraded the transmitted spectra to UVIS resolution by using a Gaussian LSF with a standard deviation of 1.2 Å (see Section 2.1). We then binned the fluxes into UVIS pixels and used the UVIS calibration algorithm in reverse to convert the fluxes into detector counts. Because the S/N of the UVIS data is worse than the S/N of the IUE data, we added random noise to each transmitted spectrum separately in order to simulate the larger uncertainty in accordance with Eq. (2).

The procedure described above yields synthetic stellar spectra at each impact parameter as would be observed during a real occultation. We calculated transmission based on the synthetic data by using the procedure outlined in Section 2.1 and retrieved column density and number density profiles from the transmission spectra by using the methods introduced in Section 2.2. Fig. 3 demonstrates that the synthetic light curves and spectra are a good representation of the real data. It shows a synthetic light curve for $\lambda_p = 1500.46$ Å, which can be compared with the real data for $a > 1650$ km in Fig. 2, and a synthetic spectrum of optical depth averaged over $a = 700$ –750 km, which can be compared with the real data in Fig. 11. The results illustrate that the synthetic noise and count rate agree well with the observed signal. They also show that the chosen absorbers and model abundances are appropriate for modeling extinction in the upper atmosphere of Titan.

Fig. 4 contrasts the column densities retrieved from the synthetic occultation with the original model profiles. The results imply that the LM fits are accurate for retrieving the column densities of CH_4 , C_2H_2 , C_4H_2 , C_6H_6 and HC_3N within the altitude ranges given in Table 2. In general, the error calculated by the LM algorithm is also consistent with the expected results within the valid altitude range. The HCN retrieval is more uncertain because it relies on a few sharp absorption lines near 1410 Å in the cross section that overlap with absorption by other species (see Section 3.2). However, the input model profiles are still consistent with the error in the retrieval between $a \approx 500$ –1000 km. In general, it should be assumed that the retrieval is accurate within the 3σ uncertainty. This is not the case for C_2H_6 at $a > 700$ km because its absorption cross section overlaps with that of CH_4 and it has no clear absorption lines that can be identified in the data. The retrieved column density profile of C_2H_6 deviates significantly from the model at high altitudes. In this case the error calculated by the LM algorithm is clearly incorrect. This raises a question about the general validity of the error estimates, but these simulations do provide a guide to where the analysis of the real data can be trusted. A more comprehensive error analysis may be required to verify them in the future. We note that including C_2H_6 in the retrievals at altitudes where it cannot be properly constrained can change the density profiles of CH_4 and HC_3N .

Fig. 5 shows the number densities based on inverting the column density profiles with Tikhonov regularization. In general, the inversion performs well if the column density profiles span a

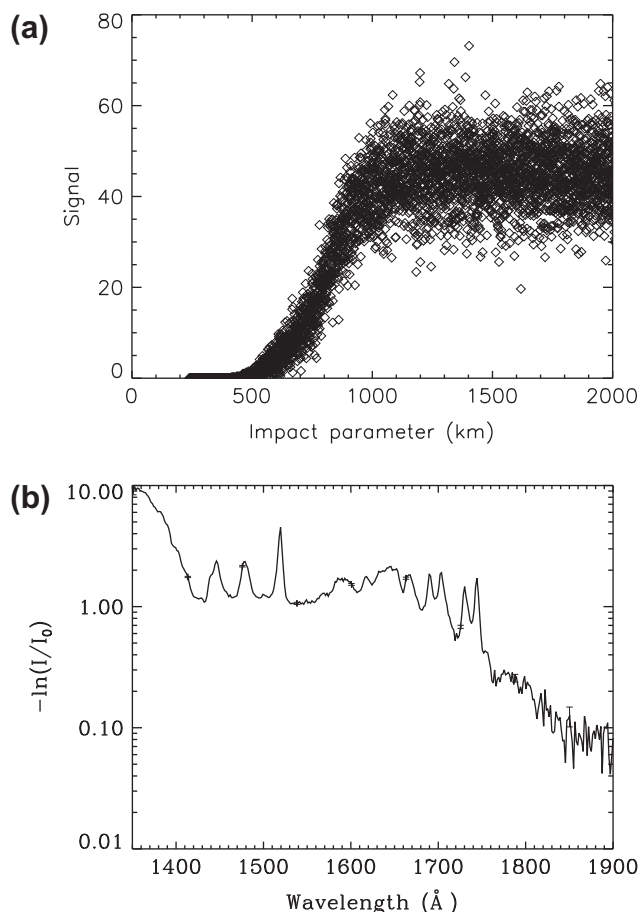


Fig. 3. (a) Synthetic light curve based on the T41 I occultation for a single pixel centered at $\lambda_p = 1500.46$ Å (see Fig. 2 to compare the noise and count rate with the real data at $a > 1650$ km). (b) Spectrum of optical depth averaged over $a = 700$ –750 km based on synthetic data (see Fig. 11 for comparison).

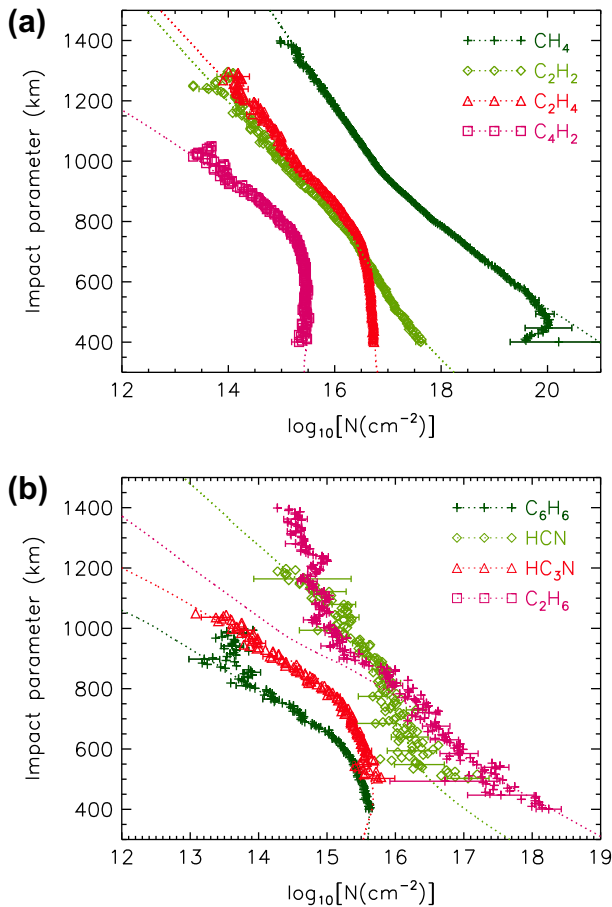


Fig. 4. Column density profiles retrieved from synthetic T41 I data. Dotted lines show the input model profiles. The altitude ranges for reliable retrieval of the density profiles for different species based on these results are listed in Table 2.

reasonable range of altitudes. As indicated by Eq. (11), the number density n_j at altitude z_j is related to row j of the retrieval gain matrix G_{ji} , which is known as the contribution function. The approximate width of the contribution function is a measure of the required span of the column density profiles for the inversion to be reliable. Our analysis of the synthetic occultations indicates that the profiles should span at least 200–300 km with a reasonable altitude resolution to facilitate reliable inversions. We note that this requirement is not universal – it depends on the vertical pressure scale of the atmosphere and the given range is therefore specific to Titan. In the current simulation, we adopted an altitude resolution of 4 km for the column densities. The rows of the averaging kernel matrix $(GA)_{ji}$ provide an estimate of the altitude resolution of the number density profiles. The kernel functions are approximately Gaussian and they are centered around the relevant altitude point z_j . We estimated the altitude resolution by fitting the functions with Gaussian distributions after the inversion and evaluating the full width half maximum (FWHM) of these distributions. Our analysis indicates that the altitude resolution of the retrieved density profiles varies between 20 and 40 km, depending on the number of iterations and the value of the regularization parameter. The choice of these parameters depends on the quality of the column density profiles. Again, it should be assumed that the densities are accurate within the 3σ confidence interval.

As indicated in Section 3.3, the density profiles of the minor species in Titan's atmosphere contain large wave-like features. It is important to verify that the retrieval captures the magnitude and structure of these features accurately because this is crucial

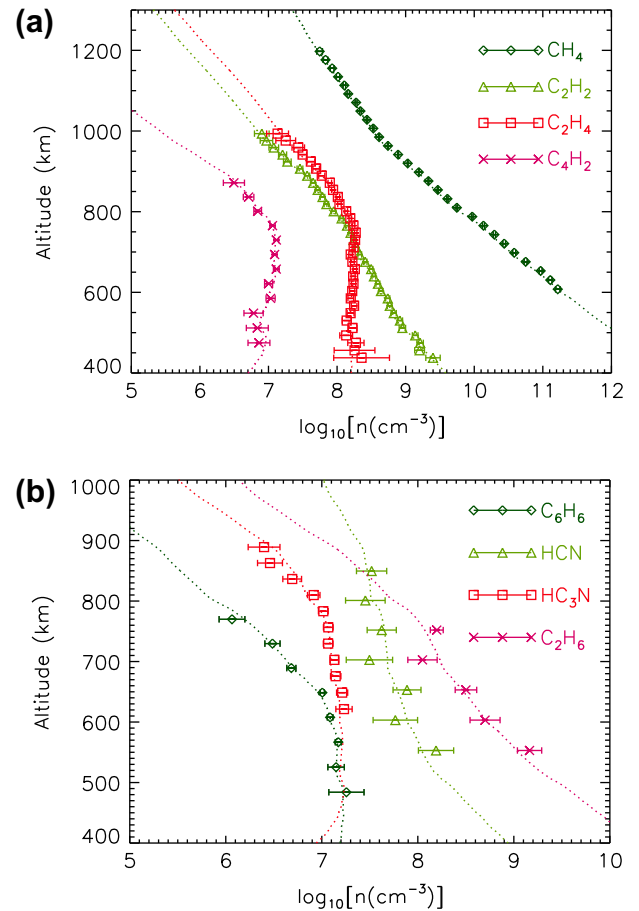


Fig. 5. Number density profiles retrieved from synthetic T41 I data. Dotted lines show the input model profiles.

to understanding their origin (see Section 4). In order to do this, we perturbed the density profiles of C_2H_2 , C_4H_2 , C_2H_4 , C_6H_6 , HCN , and HC_3N with a sinusoidal wave that has a vertical wavelength of 200 km and an amplitude corresponding to 75% of the mean density at each altitude. We then generated a new synthetic occultation based on the perturbed density profiles and retrieved them from the data with the usual methods. As an example, Fig. 6 contrasts the retrieved density profiles of C_2H_4 with the input model profiles. The results illustrate that the retrieval is accurate even in the presence of large perturbations in the density profiles.

Retrieving the density profiles of the aerosols is complicated because the FUV extinction cross sections derived from the optical properties of Khare et al. (1984) tholins are featureless and it can be difficult to distinguish extinction by aerosols from absorption by hydrocarbons and nitriles (see Section 3.2). We used the LM fits to retrieve column densities of the aerosols from synthetic data, assuming that the aerosols are spherical and have a mean radius of $r_a = 12.5$ nm at all altitudes. This is not necessarily a realistic description of the aerosols but sufficient for testing the retrieval algorithm. Fig. 7 shows the retrieved column density profile together with the original optical depth profile divided by the cross section of the spherical aerosols. The results show that the LM method is a reliable method for separating extinction by tholins from absorption by gaseous species below $a \sim 1000$ km. It should be noted, though, that the quality of the fit relies on wavelengths between 1850 and 1900 Å where few other species in the fit are absorbing. If other absorbers are present in this region, the retrieval can be more complicated.

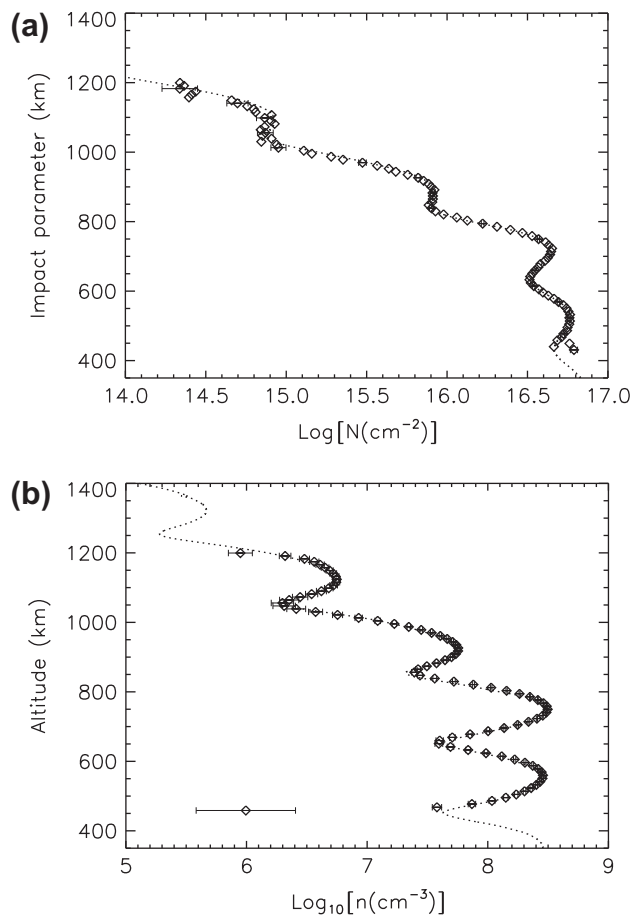


Fig. 6. (a) Column density profile and (b) number density profile of C_2H_4 retrieved from synthetic T41 I data. A sinusoidal fluctuation with a vertical wavelength of 200 km and an amplitude corresponding to 75% of the mean density was introduced to the model profiles shown by the dotted lines.

3. Results

3.1. Extinction layers

Fig. 8 shows optical depth as a function of wavelength and impact parameter for the T41 I and T53 occultations. The T41 I occul-

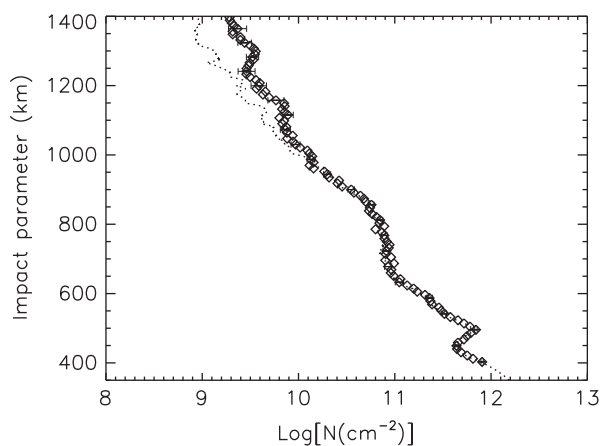


Fig. 7. Column density profile of spherical tholins with a radius of $r_a = 12.5$ nm retrieved from synthetic T41 I data. The input column density profile is shown by the dotted lines.

tation is characterized by two sharp extinction layers (regions of enhanced optical depth) centered around 500 km and 725 km, and possibly other smaller features between these layers. The T53 occultation, on the other hand, is characterized by a broad extinction layer centered around 600 km and another smaller layer near 450 km. Light curves for the other stellar occultations available from the PDS archive are shown in Fig. 9, which shows that the extinction layers appear as local minima in the transmission curves. Generally, there are two types of occultations. Some occultations are similar to T41 I in that they have extinction layers near 500 km and at higher altitudes between 700 and 800 km while others are similar to T53, with one broad layer near 600 km. It is interesting to note that occultations after T48 have another smaller layer centered near 450 km. As we demonstrate below, this layer is the detached haze layer that shifts to a lower altitude around the equinox of 2009.

The 500 km layer in panel (a) of Fig. 9 clearly coincides with the detached haze layer that was seen in images obtained by the Cassini Imaging Science Subsystem (ISS) (Porco et al., 2005). This feature appears in the λ Sco occultation (Tb II) and consequently both Shemansky et al. (2005) and Liang et al. (2007) suggested that it may be caused by aerosol extinction. This was also assumed by Lavvas et al. (2009) who used the UVIS extinction data together with ISS measurements of scattered sunlight to characterize the aerosols within the layer. At first, the lack of this layer in some of the occultations appears to challenge the idea that the detached

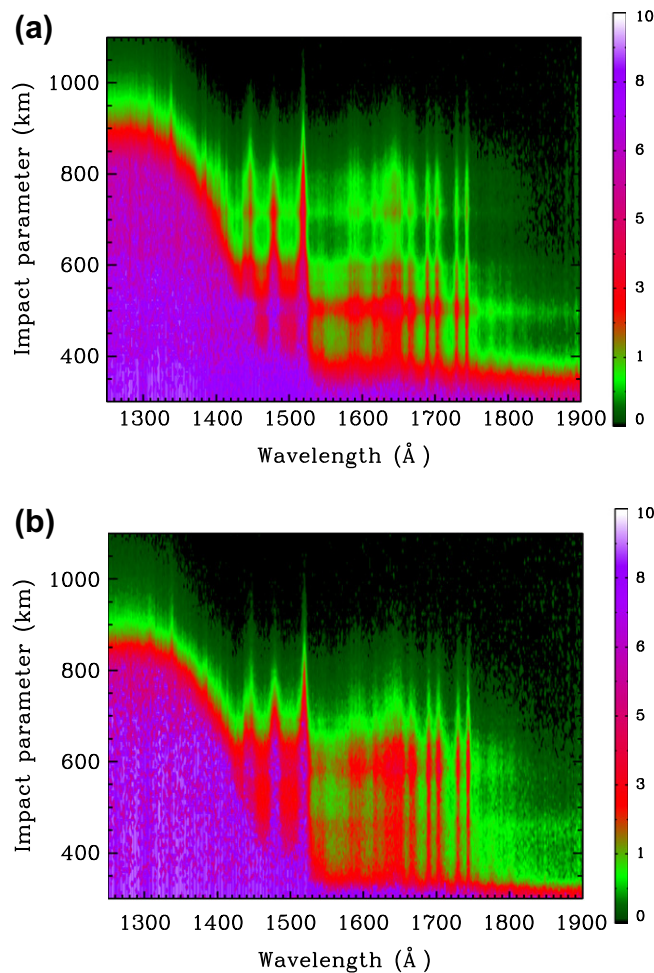


Fig. 8. Optical depth contours for T41 I (a) and T53 (b). Extinction layers (layers of higher optical depth) are marked by enhanced absorption due to both aerosols and minor species.

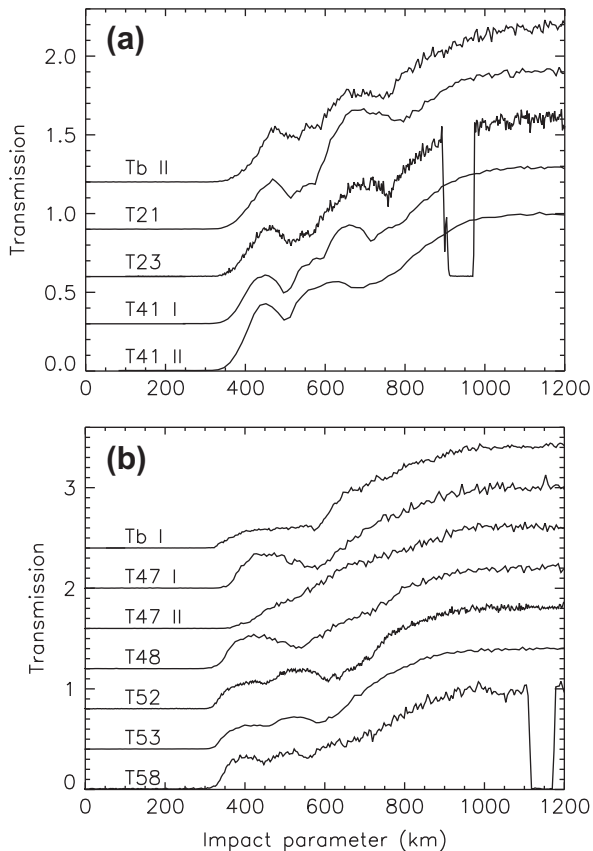


Fig. 9. Transmission averaged over 1700–1800 Å as a function of impact parameter for different occultations. The occultations in panel (a) are characterized by two distinct layers centered around 500 km and 700–800 km while the occultations in panel (b) are characterized by a broad layer centered around ~600 km. Note that T47 II has no distinct layers. The T21 and T58 occultations include data drop outs due to the star drifting out of the field of view of the spectrograph slit. The zero level of the transmission curves has been shifted by different amounts for clarity.

haze layer can be seen in the UVIS data. However, a more careful analysis shows that the low altitude layers generally coincide with the detached haze layer. The ISS images from flyby Tb show that the detached haze layer merges with the main haze layer near the north polar region and that its altitude decreases with increasing northern latitude above 30°N. Both Tb I and T47 II probe high northern latitudes and this explains the lack of a clear 500 km layer in these occultations. It is surprising that the detached haze layer is apparently not present in the T47 I and T48 occultations that probe low northern latitudes. However, both of these occultations contain a much broader extinction layer that includes the 500 km layer and could be masking it from view.

More recent ISS images indicate that the detached haze layer underwent a rapid change in altitude near the equinox of 2009 (West et al., 2011). This affected its location in the T52, T53, and T58 occultations because these flybys took place close the equinox. All of these occultations contain an extinction layer between 430 and 480 km. We show in Section 3.4 that the optical depth profile of the aerosols derived from the T53 data has a peak near 450 km. Therefore, our results indicate that the detached haze layer had shifted down to ~450 km by April 2009 at least at northern latitudes and by July 2009 even at southern latitudes. This is illustrated by Fig. 10 that shows the altitude of the detached haze layer in the ISS images as a function of time (West et al., 2011) together with the altitudes obtained from the UVIS data. It demonstrates that the altitudes of the detached haze layer in the UVIS data and ISS images are consistent with each other between 2004 and 2009.

Extinction within the layers is not only due to aerosols. The density profiles of the gaseous absorbers also contain strong perturbations that coincide with the extinction layers. In particular, the 700–800 km layer that appears in some of the occultations, and the broad 600 km layer are mostly caused by significant perturbations in the density profiles of the minor species that depend on time and/or latitude. In order to separate extinction by aerosols from absorption by hydrocarbons and nitriles, we performed a detailed analysis of the transmission spectra derived from T41 I and T53 occultations. In Section 3.2 below we show that the data can be fitted with a reasonable combination of aerosols and gaseous species. Our analysis demonstrates that the extinction profiles of the aerosols and gaseous species both contain perturbations that give rise to the extinction layers in the light curves.

3.2. Minor species

Shemansky et al. (2005) used the Tb λ Sco and α Vir occultations to identify CH₄, C₂H₂, C₂H₄, C₂H₆, C₄H₂, and HCN in the UVIS data. Liang et al. (2007) used the same data to study the properties of high altitude aerosols on Titan (see also Lavvas et al., 2009). They concluded that the aerosol cross section has a wavelength dependency proportional to $\lambda^{-1.5}$. Assuming that the aerosols have the optical properties of solid laboratory tholins (Khare et al., 1984), they derived a density profile for the aerosols between 500 and 1000 km. This resulted in the detection of aerosols at altitudes as high as 1000 km in Titan's thermosphere. Later, Ferradaz et al. (2009) argued that HC₃N may also be detectable in the data. They also showed that using up to date measurements of the absorption cross sections leads to a better fit to the C₄H₂ features. In this section we discuss the identification of different absorbers based on the T41 I occultation. We confirm that HC₃N is detectable and identify C₆H₆ in the data. We also show that due to confusion with other absorbers, the data place only loose constraints on the wavelength dependency of aerosol extinction.

3.2.1. Extinction around the 725 km layer

We fitted column densities to the data with a combination of CH₄, C₂H₂, C₂H₄, C₄H₂, C₂H₆, C₆H₆, HCN, HC₃N and aerosols by using the LM algorithm discussed in Section 2.2. In line with Liang et al. (2007), we assumed that the aerosols are spherical with a radius of $r_a = 12.5$ nm and that they have the optical properties of tholins. Note that we chose this radius for illustration purposes only – the wavelength dependency of the aerosol cross section does not

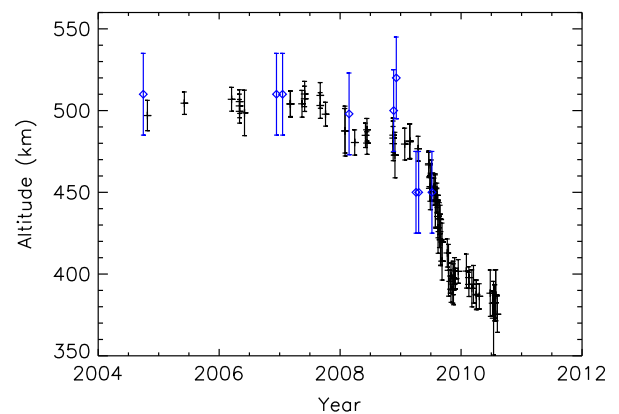


Fig. 10. The observed altitude of the detached haze layer as a function of time based on Cassini/ISS measurements by West et al. (2011) (crosses) and UVIS data (diamonds). The error on the UVIS points was estimated from the approximate width of the 450–500 km extinction layer in the data.

change significantly with size, given a feasible range of radii between $r_a \approx 5\text{--}40$ nm at $a = 500\text{--}1000$ km (see Section 3.4). Fig. 11 shows the spectrum of optical depth for the T41 I occultation averaged over impact parameters between $a = 700\text{--}750$ km. It also shows the optical depth contributions from different absorbers and normalized optical depth residuals based on the best fit. The latter are given by $(\tau_d - \tau_m)/\sigma$ where τ_d is the observed optical depth, τ_m is the model depth, and σ is the measurement error. We chose this altitude region for illustration purposes because it coincides with the 725 km extinction layer. The column densities based on the fit are shown in Table 3. As indicated by Fig. 11, the spectrum contains easily recognizable absorption lines of CH_4 , C_2H_2 , C_4H_2 and C_2H_4 but the identification of C_2H_6 , C_6H_6 , HCN , HC_3N and tholins is based on less distinct features. In order to verify the identification of these species in the data, we removed them one by one from the forward model and explored the quality of the resulting fit.

The best fit to the average data at $a = 700\text{--}750$ km with all of the above absorbers yields a value for reduced chi squared of $\chi_v^2 = 5.9$. Removing C_6H_6 and recalculating the best fit based on the remaining species increases this value to $\chi_v^2 = 8.4$. We performed the F test to assess the statistical significance of the detection of C_6H_6 by calculating $F_\chi = \Delta\chi^2/\chi_v^2$ based on fits that excluded and included C_6H_6 . The value of $F_\chi = 350$ indicates that the detection is statistically significant. This can be seen in Fig. 12, which shows the optical depth residuals for the best fit without C_6H_6 and the absorption cross section of C_6H_6 that was scaled to match with the residuals. The residuals contain a broad absorption band centered around 1790 Å that agrees with the cross section of C_6H_6 and cannot be fitted with aerosols alone. As indicated by Fig. 11, this feature disappears when C_6H_6 is included in the fit.

Ferradaz et al. (2009) pointed out that the absorption lines of HC_3N and C_4H_2 overlap between 1350 and 1500 Å, making them difficult to separate. However, they argued that HC_3N can be

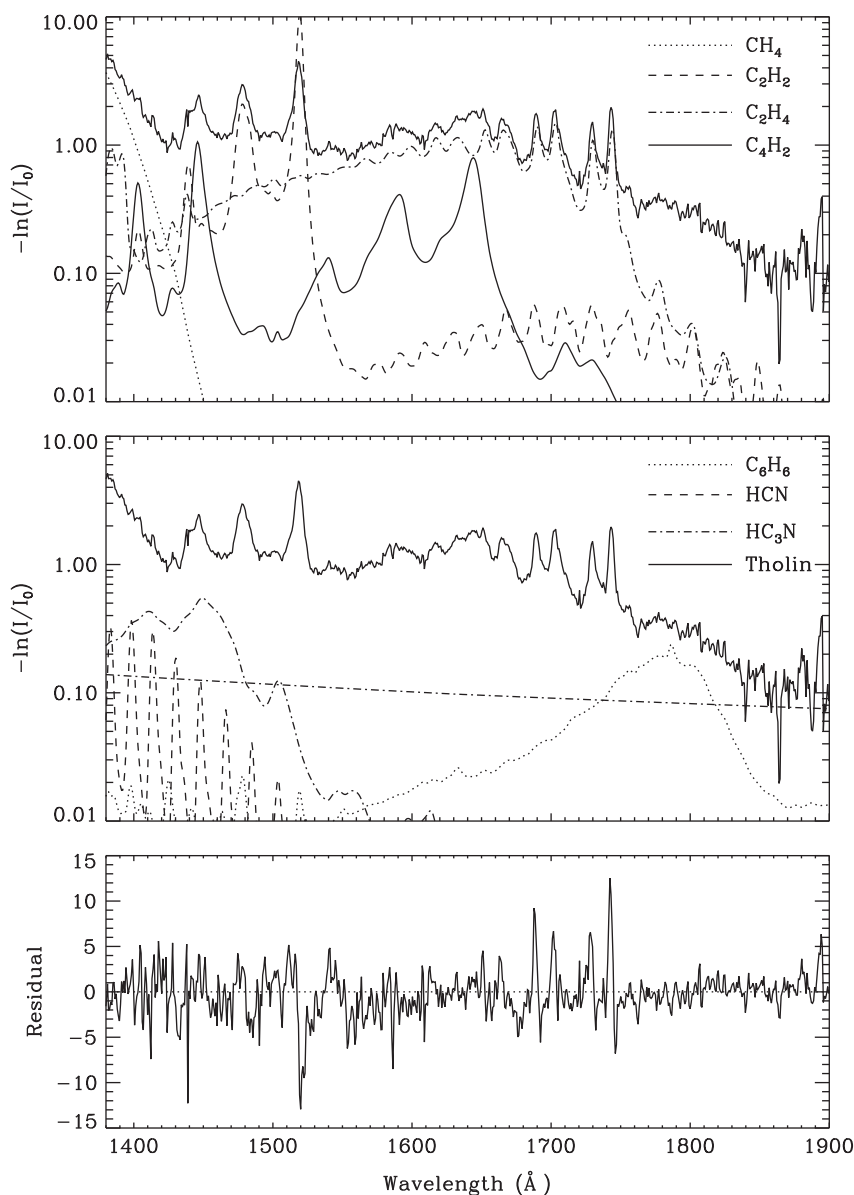


Fig. 11. Spectrum of optical depth averaged over $a = 700\text{--}750$ km based on the T41 I data. The solid lines in the two upper panels show the data and the other lines show contributions from different absorbers based on best fit column densities listed in Table 3 and absorption cross sections listed in Table 2. The third panel shows the normalized best fit optical depth residuals [defined as $(\tau_d - \tau_m)/\sigma$ where τ_d is the observed optical depth, τ_m is the model depth, and σ is the measurement error] based on absorption by CH_4 , C_2H_2 , C_2H_4 , C_4H_2 , C_2H_6 , C_6H_6 , HCN , HC_3N and aerosols. In this case, we assumed that the aerosols are spherical with a radius of $r_a = 12.5$ nm. The optical depth of C_2H_6 is not shown because it is only an upper limit at this altitude.

Table 3
Best fit column densities in the extinction layers of T41 I.

Species	N_s (cm ⁻²) 500–550 km	N_s (cm ⁻²) 700–750 km
CH ₄	N/A	$(1.6 \pm 0.03) \times 10^{18}$
C ₂ H ₂	$(1.8 \pm 0.04) \times 10^{17}$	$(3.4 \pm 0.05) \times 10^{16}$
C ₂ H ₄	$(3.9 \pm 0.04) \times 10^{16}$	$(2.5 \pm 0.02) \times 10^{16}$
C ₄ H ₂	$(3.3 \pm 0.1) \times 10^{15}$	$(1.7 \pm 0.05) \times 10^{15}$
C ₂ H ₆	$(5.5 \pm 0.2) \times 10^{17}$	$< 2.7 \times 10^{16}$
C ₆ H ₆	$(6.6 \pm 0.3) \times 10^{14}$	$(7.8 \pm 0.3) \times 10^{14}$
HCN	N/A	$(2.3 \pm 0.2) \times 10^{16}$
HC ₃ N	N/A	$(2.4 \pm 0.06) \times 10^{15}$
Tholins ^a	$(5.3 \pm 0.7) \times 10^9$	$(7.7 \pm 0.3) \times 10^{11}$

^a The radii of the spherical tholins were assumed to be $r_a = 40$ nm at $a = 500$ – 550 km and $r_a = 12.5$ nm at $a = 700$ – 750 km (see text).

detected with sufficient S/N because its presence affects the relative intensity of the main absorption bands of C₄H₂ in the transmission data. We note that the T41 I data have the best S/N and this occultation is therefore the best candidate for this type of identification. Indeed, removing HC₃N leads to $\chi^2_v = 8.5$ and $F_\chi = 370$ between the fits that exclude and include HC₃N. Fig. 13 shows the optical depth residuals for the fit that does not include HC₃N together with the scaled absorption cross section of HC₃N. Compared to the residuals in Fig. 11, it shows missing absorption in the model near the $^1\Sigma_u^+ - ^1\Sigma_g^+$ transition (~ 1450 Å) of HC₃N, the strongest band in its FUV spectrum. This confirms the detection of HC₃N as statistically significant.

The absorption lines of HCN at $\lambda_p < 1500$ Å overlap with those of C₂H₆, C₄H₂, C₂H₄ and C₂H₂. The only feature that stands alone is the peak near 1410 Å (see Fig. 11) that appears consistently at several altitudes in different occultations. Removing HCN from the fit leads to $\chi^2_v = 6.7$ and $F_\chi = 107$ between the fits that exclude and include HCN. Fig. 14 shows the optical depth residuals and scaled absorption cross section of HCN for the fit that does not include HCN. It shows missing absorption in the forward model that coincides with some absorption lines of HCN at $\lambda_p < 1500$ Å. The detection of HCN is thus statistically significant near 725 km, although less so than the detection of HC₃N.

We also removed C₂H₆ from the fit. The transmission spectrum does not contain any clearly identifiable absorption lines of C₂H₆ but Cassini INMS measurements show that its mixing ratio is $(7.3 \pm 2.6) \times 10^{-5}$ near 1080 km (Cui et al., 2009). Photochemical

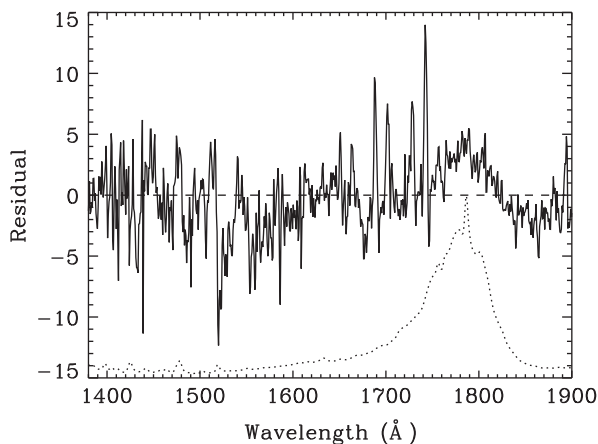


Fig. 12. Normalized optical depth residuals (solid line) of a model fit ($\chi^2_v = 8.4$) based on absorption by CH₄, C₂H₂, C₄H₂, C₂H₄, C₂H₆, HCN, HC₃N and tholins. The data were averaged between $a = 700$ – 750 km. The dotted line shows the scaled absorption cross section of C₆H₆. The residuals point to significant missing absorption in the forward model that coincides with absorption by C₆H₆ and thus shows that it is detectable in the data.

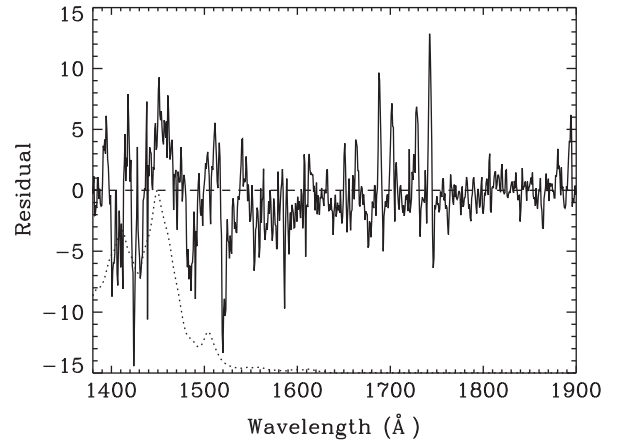


Fig. 13. Normalized optical depth residuals (solid line) of a model fit ($\chi^2_v = 8.5$) based on absorption by CH₄, C₂H₂, C₄H₂, C₂H₄, C₂H₆, HCN, C₆H₆ and tholins. The data were averaged between $a = 700$ – 750 km. The dotted line shows the scaled absorption cross section of HC₃N. The residuals reveal missing absorption in the forward model associated with the $^1\Sigma_u^+ - ^1\Sigma_g^+$ transition of HC₃N.

calculations indicate that the mixing ratio should range between 10^{-5} and 10^{-4} at altitudes of 400–1000 km (e.g., Lavvas et al., 2008b) and similar mixing ratios were derived from Cassini/CIRS data for altitudes below 400 km (Vinatier et al., 2010a). Based on these constraints, the expected column density of C₂H₆ between 700 and 750 km is 7×10^{15} cm⁻². This column density is not high enough to produce significant absorption in the data. In fact, removing C₂H₆ does not affect the fit – it does not change χ^2_v at all. As indicated by the data simulation in Section 2.3, only upper limits can be derived for the column density of C₂H₆ at $a = 700$ – 750 km. We derived this upper limit by increasing the column density of C₂H₆ until χ^2_v reached 6.9 and listed the resulting value in Table 3.

Lastly, we explored the contribution of aerosols. Fig. 11 shows the featureless extinction cross section of the Khare et al. (1984) tholins that, together with a small contribution from C₆H₆, are responsible for extinction between 1850 and 1900 Å. Removing the aerosols from the fit leads to $\chi^2_v = 6.5$ and $F_\chi = 87$ between

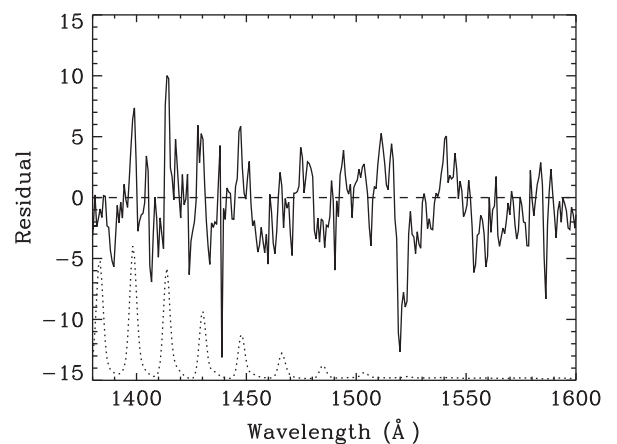


Fig. 14. Normalized optical depth residuals (solid line) of a model fit ($\chi^2_v = 6.7$) based on absorption by CH₄, C₂H₂, C₄H₂, C₂H₄, C₂H₆, C₆H₆, HC₃N and tholins. The data were averaged between $a = 700$ – 750 km. The dotted line shows the scaled absorption cross section of HCN. The residuals point to missing absorption in the forward model that coincides with absorption lines of HCN. Note that absorption lines at wavelengths shorter than 1400 Å are not detectable because the atmosphere is impenetrable for UV light in that region at the given range of impact parameters.

the fits that exclude and include aerosols. These values indicate that the detection of aerosols is statistically significant. This is illustrated by Fig. 15, which shows the residuals for the fit that excludes aerosols. It indicates that the forward model fails to fit the spectrum satisfactorily at $\lambda_p > 1800 \text{ \AA}$ when aerosols are excluded. However, the two unidentified absorption lines between 1870 and 1900 \AA complicate this picture. These features represent 4–6 σ deviations from the fit. They are present at all altitudes in the T41 I data where atmospheric absorption is detected. The S/N of the T53 data is slightly worse and the features represent only 2–4 σ deviations but are still present. They are not prominent in occultations obtained during flybys other than T41 I and T53 because high S/N is required to see them. It should also be noted that the features are located in a region of the spectrum where the true error may be larger than that implied by Eq. (2) (see Section 2.1).

The presence of unidentified absorption lines raises the prospect of other absorbers being responsible for extinction in the 1850–1900 \AA region in addition to aerosols. In fact, several hydrocarbon and nitrile species have cross sections with prominent absorption lines in this region. For instance, photochemical calculations indicate that the column density of C_6H_2 , which has a broad absorption feature centered between 1800 and 1900 \AA , should be comparable to that of C_6H_6 near 750 km (Lavvas et al., 2008b). Other possible absorbers include, for instance, $(\text{CH}_3)_2\text{C}_6\text{H}_5$ (toluene) and (m,o,p)- $(\text{CH}_3)_2\text{C}_6\text{H}_4$ (xylene). These species are formed by replacing H atoms in the C_6H_6 rings with CH_3 radicals. Thus, similar to C_6H_6 , their cross sections are characterized by a broad absorption band near 1800–1900 \AA with some additional features. They are interesting because C_6H_6 is abundant in the thermosphere (Vuitton et al., 2008) and in the UVIS data. CH_3 , on the other hand, is the most abundant radical in the photochemical models and its attachment to C_6H_6 could constitute a first step towards the formation of more complex molecules. In this respect, p- $(\text{CH}_3)_2\text{C}_6\text{H}_4$ is particularly interesting because its cross section contains two peaks that agree broadly with the unidentified features in the data. Unfortunately, neither the published cross section for this species (Suto et al., 1992) or the UVIS data at these wavelengths are of high enough quality to support more definite conclusions.

3.2.2. Extinction around the 500 km layer

Fig. 16 shows the spectrum of optical depth averaged over impact parameters between $a = 500$ –550 km. It also shows the optical depth contributions from different absorbers and residuals based on a fit that includes C_2H_2 , C_2H_4 , C_4H_2 , C_2H_6 , C_6H_6 and aerosols.

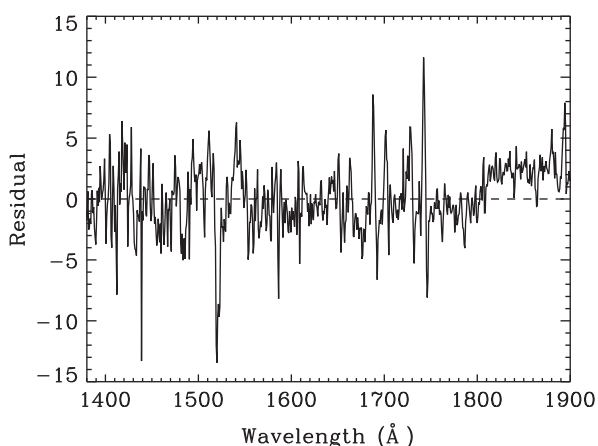


Fig. 15. Normalized optical depth residuals (solid line) of a model fit ($\chi_v^2 = 6.5$) based on absorption by CH_4 , C_2H_2 , C_4H_2 , C_2H_4 , C_2H_6 , HCN, HC_3N and C_6H_6 . The data were averaged between $a = 700$ –750 km. The exclusion of aerosols from the model leads to missing absorption at $\lambda_p > 1800 \text{ \AA}$ and slight excess absorption by C_6H_6 .

This altitude range was chosen because it coincides with the detached haze layer. The best fit column densities that yield $\chi_v^2 = 2.8$ are listed in Table 3. In this case, we assumed that the aerosols are spherical with a radius of $r_a = 40 \text{ nm}$ that is appropriate for the detached haze layer (Lavvas et al., 2009). The exclusion of HCN and HC_3N from the model does not affect the results because the transmission spectrum is saturated at $\lambda_p < 1450 \text{ \AA}$ and thus the significant absorption lines of these species are not visible. By saturation in this context we mean that the optical depth in this region of the spectrum is high enough to absorb practically all of the stellar flux. We note that the spectrum is also saturated in the strong absorption lines of C_2H_2 near 1480 \AA and 1520 \AA and thus the apparent excess absorption produced by the model in these lines is not a problem because the true optical depth of the atmosphere is higher than that implied by the data in Fig. 16.

Removing C_2H_6 from the best fit for the 500 km detached haze layer leads to $\chi_v^2 = 3.4$ and $F_\chi = 175$ between the models that exclude and include C_2H_6 . This result is surprising because, due to saturation at $\lambda_p < 1520 \text{ \AA}$, the retrieval relies on matching the extended slope and absorption bands in the cross section of C_2H_6 at wavelengths shorter than 1550 \AA with the data in Fig. 16. However, it agrees with the data simulation in Section 2.3, which indicates that the column density of C_2H_6 can be retrieved satisfactorily for $a = 500$ –700 km. Despite this statistical detection of C_2H_6 , we note that the retrieved densities of both CH_4 and C_2H_6 should be treated with caution at altitudes below $\sim 650 \text{ km}$.

It is interesting to note that, compared to $a = 700$ –750 km, aerosols are detected with higher confidence at $a = 500$ –550 km. Removing the tholins from the fit leads to $\chi_v^2 = 21$ and produces large optical depth residuals that are shown in Fig. 17. In addition to leading to a worse fit at $\lambda_p > 1800 \text{ \AA}$, the exclusion of aerosols also causes problems at shorter wavelengths where significant ‘background’ extinction by aerosols is required to fit the spectral lines of the minor species. This implies that, as expected, aerosol extinction is significant near and above the detached haze layer. Further, the opacity of the aerosols increases significantly with decreasing altitude below 700 km.

We note that χ_v^2 statistics cannot be used to obtain strong constraints on the wavelength dependence and thus the size of the aerosols in the haze layers. In order to show this, we excluded tholins from the model and instead assumed that the extinction cross section of the aerosols varies simply as $\sigma_e \propto \lambda_p^{-\alpha}$. Having done this, we recalculated the LM fits by treating the proportionality constant and α as free parameters. We found that values of $\alpha = 0$ –2.5 lead to practically identical values of χ_v^2 both for $a = 500$ –550 km and $a = 700$ –750 km. On this basis, values of $\alpha > 2.5$ are excluded by the data. The extinction cross sections of the tholins we used in this study are consistent with this constraint (see Section 3.4).

The strong absorption bands of C_2H_2 , C_2H_4 , C_4H_2 are clearly visible in the data and their presence at $a = 500$ –550 km does not need to be tested further. Instead, we verified that C_6H_6 is still detectable. Removing it leads to $\chi_v^2 = 3.6$ and $F_\chi = 219$ between the models that exclude and include C_6H_6 . Thus the detection of C_6H_6 is statistically significant at $a = 500$ –550 km. Fig. 18 shows the optical depth residuals for the best fit without C_6H_6 . Again, they include the broad absorption band of C_6H_6 centered around 1790 \AA .

With $\chi_v^2 = 5.9$ at $a = 700$ –750 km and $\chi_v^2 = 2.6$ at $a = 500$ –550 km, the best fits are good but not perfect. Fig. 11 shows that the largest discrepancies between the model and the data appear within the narrow absorption lines of C_2H_2 and C_2H_4 . These problems also appear at the lower range of impact parameters (see Fig. 16). The problem of fitting the strong absorption lines of C_2H_2 near 1520 \AA and 1480 \AA is not serious at 500 km because the lines are saturated and their true depth is not known. Also, the 1520 \AA absorption line of C_2H_2 is nearly saturated at 700 km.

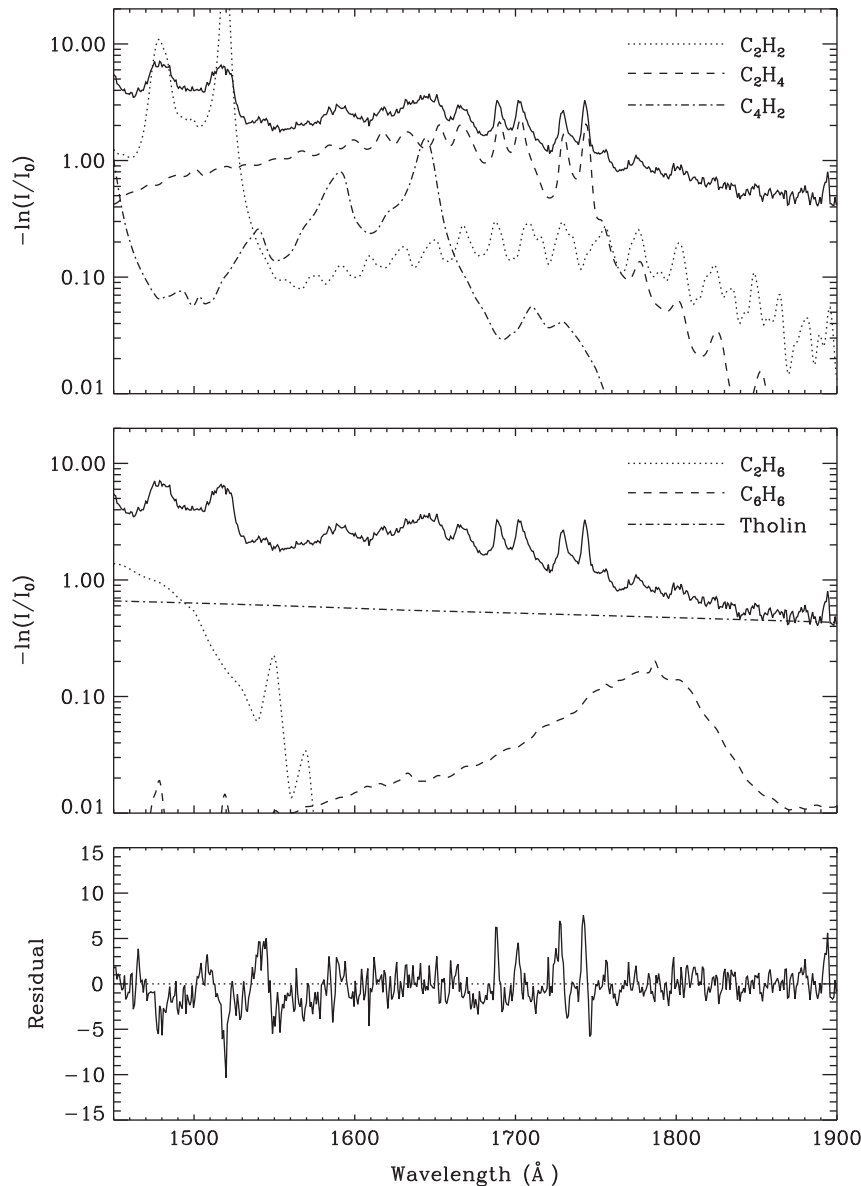


Fig. 16. Spectrum of optical depth averaged over $a = 500\text{--}550$ km based on the T41 I data. The solid lines in the two upper panels show the data and other lines show contributions from different absorbers based on best fit column densities listed in Table 3 and absorption cross sections listed in Table 2. The lower panel shows the best fit normalized optical depth residuals ($\chi^2 = 2.8$) based on absorption by C_2H_2 , C_2H_4 , C_4H_2 , C_2H_6 , C_6H_6 and aerosols. We assumed that the aerosols are spherical with a radius of $r_a = 40$ nm. Note that the excess absorption in the 1480 Å and 1520 Å absorption lines of C_2H_2 is not a problem because the transmission spectrum is saturated in these lines.

However, the fits systematically underestimate absorption within the strong absorption bands of C_2H_4 around 1700 Å. There could be several reasons for the discrepancies – here we discuss only the most obvious possibilities.

First, the wavelength resolution of the instrument that we assumed in the forward model could be inaccurate. In particular, we have ignored the extended wings of the LSF (see Section 2.1). However, this means that we have assumed a slightly better wavelength resolution than that implied by the full LSF and including the wings would only make the problem of fitting the C_2H_4 bands worse. Second, low temperatures lead to narrow absorption lines with strong cores, and using cross sections measured at a temperature higher than the temperature in the atmosphere could lead to the observed discrepancy between the model and the data within the cores of the C_2H_4 lines. However, the cross section of C_2H_4 that we use in our analysis was measured at 140 K and thus a temperature disagreement is not likely to explain the discrepancy

between the model and the data. The third possibility is that the intensities of the absorption bands in the laboratory measurements are uncertain – although the systematic uncertainty in the measurements should be smaller than 10%.

We note that the above discussion should be treated with caution because the results apply to a 50 km range of impact parameters, and the column densities of all of the species change sharply with altitude both near 525 km and 725 km. In order to retrieve column density profiles for different species, we used smaller altitude bins of $1\text{--}8$ km. Fig. 19 shows χ^2_v as a function of altitude for a retrieval with an altitude resolution of 4 km, indicating that the quality of the fit is excellent within the smaller altitude bins at all impact parameters. This means that the uncertainties on the retrieved column densities should be accurate, where appropriate, and the inclusion of unidentified absorbers later should not have a large impact on the derived values. We conclude that the detections of CH_4 , C_2H_2 , C_2H_4 , C_4H_2 , C_6H_6 , HCN , HC_3N and aerosols in the

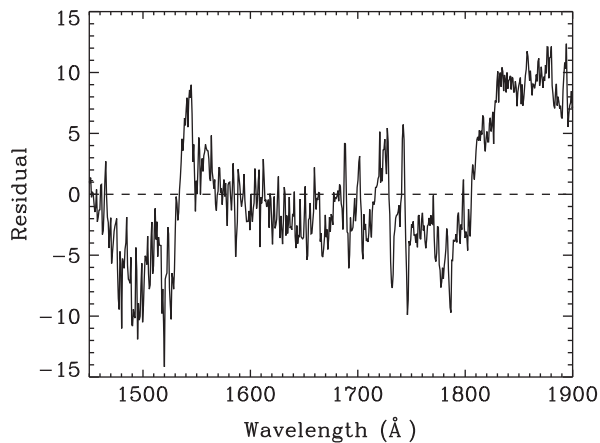


Fig. 17. Normalized optical depth residuals (solid line) for a model fit ($\chi^2 = 21$) based on absorption by C_2H_2 , C_4H_2 , C_2H_4 , C_2H_6 and C_6H_6 . The data were averaged between $a = 500$ – 550 km, i.e., within the detached haze layer. The exclusion of aerosols from the model does not only deteriorate the fit at $\lambda_p > 1800$ Å but also leads to a worse fit at shorter wavelengths.

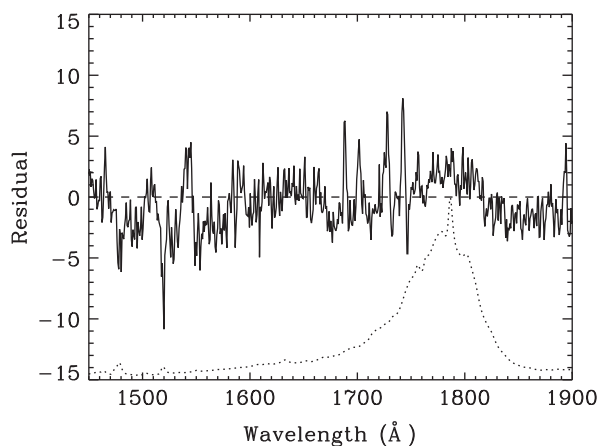


Fig. 18. Normalized optical depth residuals (solid line) for a model fit ($\chi^2 = 3.6$) based on absorption by C_2H_2 , C_4H_2 , C_2H_4 , C_2H_6 and tholins. The data were averaged between $a = 500$ – 550 km, i.e., within the detached haze layer. The dotted line shows the scaled absorption cross section of C_6H_6 . The residuals point to missing absorption by C_6H_6 near 1790 Å in the forward model.

data are secure. Extinction within the 725 km layer in the T41 I data arises mostly from hydrocarbons and nitriles, with a small contribution from aerosols. Extinction by aerosols is much stronger in the detached haze layer between $a = 500$ – 550 km. Our results indicate that the data can only be used to obtain upper limits on the column density of C_2H_6 above ~ 700 km. We discuss the retrieval of the density profiles further in Section 3.3 below.

3.3. Density profiles

In Sections 3.1 and 3.2 we argued that the extinction layers evident in the light curves arise from perturbations in the density profiles of the minor species and in the extinction profiles of the aerosols. In particular, we argued that the 725 km layer in the T41 I data and the 600 km layer in the T53 data are mostly due to hydrocarbons but that the 500 km and 450 km layers in these occultations coincide with haze layers. Here we show that, although extinction by haze is significant in the 450–550 km layers, the density profiles of the hydrocarbon species also have maxima in *both* the high and low altitude layers. This conclusion is

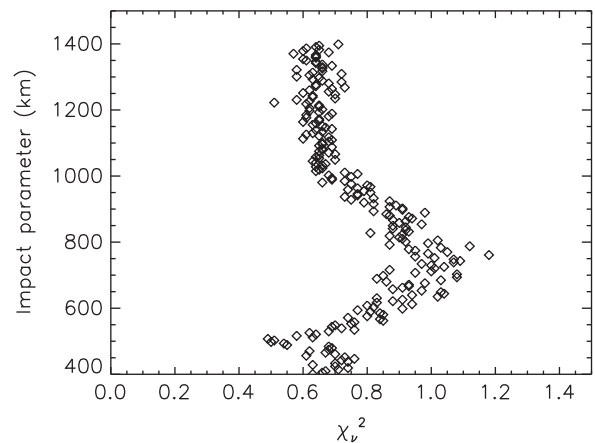


Fig. 19. χ^2 as a function of impact parameter based on the retrieval of column densities from the T41 I data with an altitude resolution of ~ 4 km. This implies binning 10 points in altitude from the original data for each grid point in the retrieval.

based on best fit density profiles of the gaseous absorbers. Further, in Section 3.4 we show that there is a distinct peak in the extinction coefficients of the aerosols associated with the 500 km and 450 km layers in the T41 and T53 data, respectively, whereas no sharp features coincide with the 725 km and 600 km layers.

Figs. 20 and 21 show the column density profiles retrieved from the T41 I and T53 data, respectively. They demonstrate that the extinction layers coincide with local maxima in the column density profiles of the minor species. Both the 500 km and 725 km layers appear in the T41 I profiles whereas only the 600 km layer is apparent in the T53 profiles. In both cases the relative density perturbations are much more prominent in the profiles of the minor hydrocarbons and nitriles than they are in the density profile of CH_4 . This means that the mechanism responsible for causing the density perturbations does not affect CH_4 in the same way as it affects the other minor absorbers.

Until now, the composition of the atmosphere between $z = 500$ – 1000 km has been largely unknown. Before the UVIS measurements presented by Shemansky et al. (2005), the only available density profiles for the minor species were based on solar occultations observed by the Voyager/UVS instrument (e.g., Broadfoot et al., 1981; Smith et al., 1982; Vervack et al., 2004). The wavelength coverage of these observations was 530–1700 Å with a spectral resolution of 18–30 Å. The altitude resolution varied between 7 and 20 km. These data were discussed by Smith et al. (1982) who only considered extinction by N_2 , CH_4 and C_2H_2 in their analysis. A thorough reanalysis by Vervack et al. (2004) led to a revision of the earlier results and the detection of C_2H_4 in the data. They also found evidence for the presence of either HCN or HC_3N but the wavelength resolution in the UVS data was not sufficient to separate the absorption features of these species from each other. The results highlighted the importance of understanding the performance of the instrument and the potentially large errors caused by exclusion of important absorbers from the analysis. In particular, the densities of CH_4 and C_2H_2 derived by Vervack et al. (2004) are lower than the original densities obtained by Smith et al. (1982) and in much better agreement with photochemical models (Wilson and Atreya, 2004).

As explained in Section 2.2, we inverted our column density profiles in order to obtain number density profiles and compared the results with Voyager/UVS and UVIS measurements, INMS density profiles for the thermosphere and CIRS mixing ratios for the stratosphere. For instance, Fig. 22 shows the density profiles of CH_4 based on the T41 I and T53 data, newly analyzed INMS data

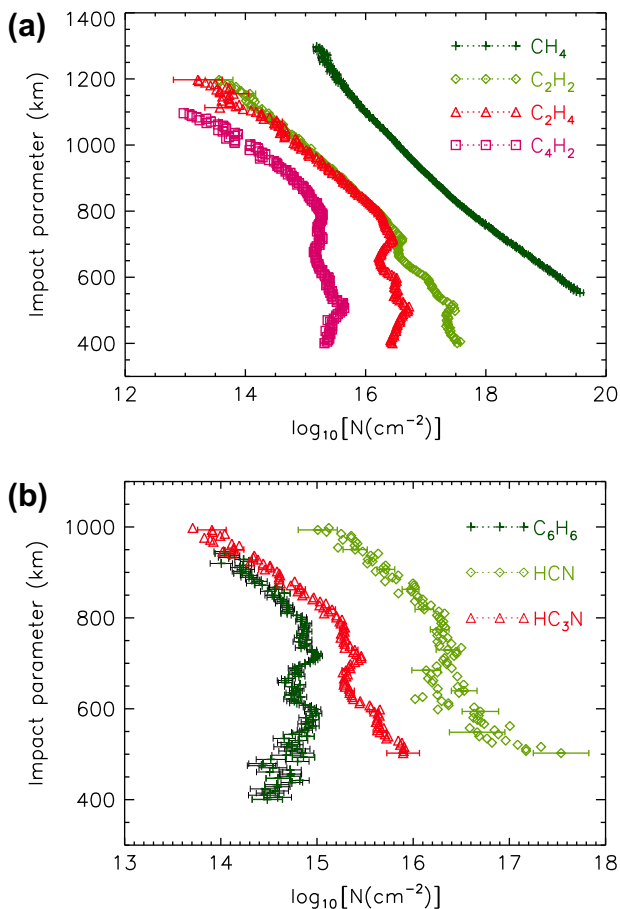


Fig. 20. Column density profiles of hydrocarbon and nitrile species retrieved from T41 I data.

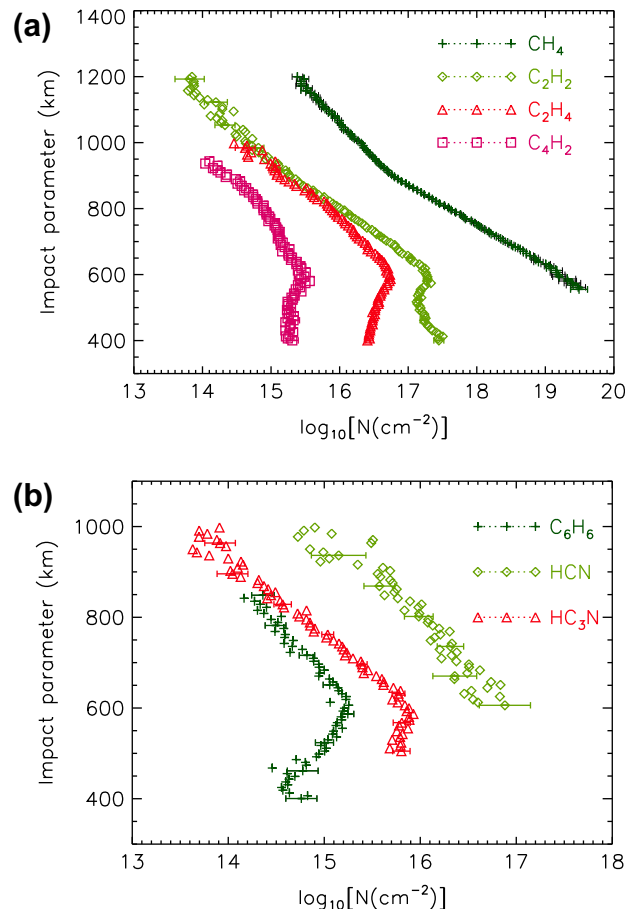


Fig. 21. Column density profiles of hydrocarbon and nitrile species retrieved from T53 data.

for flyby T41, Voyager UVS results (Vervack et al., 2004), and UVIS densities for flyby Tb (Shemansky et al., 2005). It shows that the UVS densities are comparable to the T41 densities above 1000 km and slightly higher than the T41 densities between 900 and 1000 km. Overall, the agreement between the UVS and T41 data is fairly good. The Tb densities retrieved by Shemansky et al. (2005) are in very good agreement with the T41 results below 1000 km. Above 1000 km, the Tb density does not agree with any other measurements. This is probably due to the fact that the retrieval of number densities for CH_4 based on UVIS data is generally unreliable at high altitudes.

The INMS densities of CH_4 were measured during the inbound trajectory of flyby T41 at latitudes between 34 and 44°S in the day-side. The UVIS T41 densities are ~ 2.9 times higher than the INMS densities near 1000 km and on average 3.3 times higher at altitudes between 1000 and 1200 km. This factor of ~ 3 difference is further evidence for the need to revise the INMS absolute calibration (Waite et al., in preparation). The T53 densities are comparable to T41 below 800 km but the T53 density profile differs significantly from the other measurements between 800 and 1100 km. As explained in Section 4.1, this reflects a lower temperature in this region of the atmosphere during flyby T53, and points to potentially interesting variability in the density profiles as a function of latitude and/or time.

Fig. 23 shows the density profiles of C_2H_2 based on T41 I and T53 data, Voyager UVS data (Vervack et al., 2004) and preliminary UVIS results for flyby Tb (Shemansky et al., 2005). The UVIS densities of C_2H_2 from T41 I and T53 are larger than the UVS densities at altitudes between ~ 550 and 850 km and lower than the UVS den-

sities above 850 km. The UVS densities agree well with the T53 densities above 850 km and the T41 I densities agree with the T53 densities below 550 km. This implies that the UVS and UVIS measurements agree between 400 and 500 km. The discrepancies between the UVS and UVIS densities at higher altitudes are difficult to explain. We note, however, that the UVS density is constant with altitude between 680 and 980 km, implying that the mixing ratio of C_2H_2 increases strongly with altitude there. This result is inconsistent with most photochemical models and the UVIS data. Wilson and Atreya (2004) noted that their nominal photochemical model failed to account for the low mixing ratio of C_2H_2 in the UVS data between 500 and 700 km although the model was in reasonable agreement with the other UVS measurements. They suggested that more absorption should have been ascribed to C_2H_2 in the UVS reanalysis by Vervack et al. (2004). In the light of our results, this is probably true. We note that the UVIS Tb II density of C_2H_2 (Shemansky et al., 2005) is systematically higher than either the T41 I and T53 results at altitudes higher than 700 km. This difference is not significant, however, because the reported uncertainty in the Tb II densities is 100%.

The differences between T41 I and T53 are considerable. The T41 I density profile of C_2H_2 contains a sharp and relatively narrow minimum between 650 and 700 km that also appears in the density profiles of all the other minor species other than CH_4 . Another minimum in the density profile is located just below the detached haze layer near 500 km. The T53 density profile, on the other hand, contains a deep minimum below 600 km where the density of C_2H_2 is 5–10 times lower than the T41 I density. These perturbations observed in the density profiles coincide with the extinction layers in

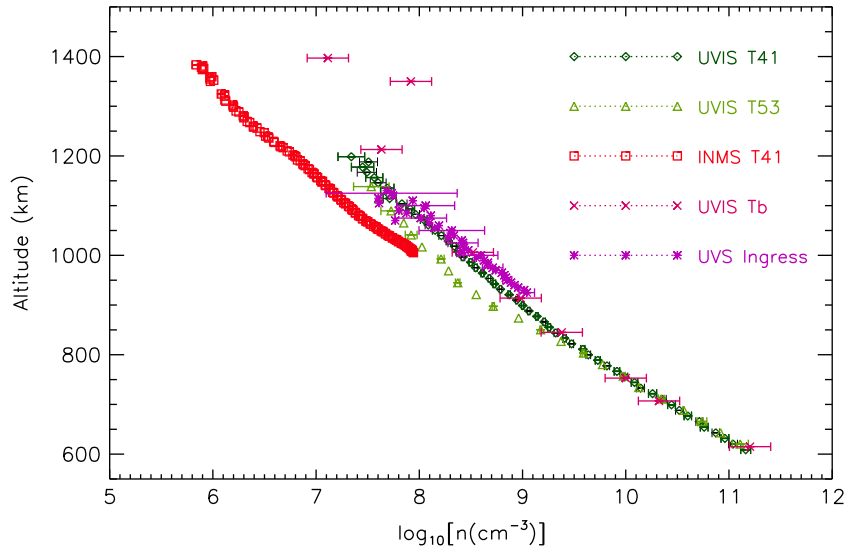


Fig. 22. Density profile of CH_4 based on different observations. The INMS densities were obtained during the inbound trajectory of flyby T41 at latitudes between 34° and 44°S during the Titan day. The UVIS Tb densities are based on the occultation of λ Sco analyzed by Shemansky et al. (2005). The UVS ingress densities are from Vervack et al. (2004). We note that the INMS T41 density is approximately 2.9 times lower than the UVIS T41 density near 1000 km and 3.3 times lower on average between 1000 and 1200 km.

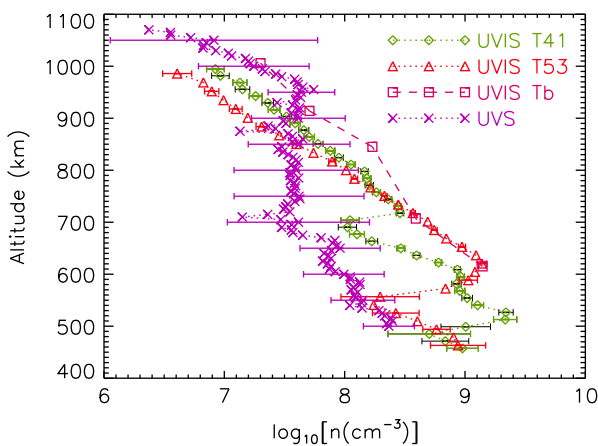


Fig. 23. Density profile of C_2H_2 based on different observations. The UVIS Tb densities are based on the occultation of λ Sco analyzed by Shemansky et al. (2005). The UVS ingress densities are from Vervack et al. (2004). Note that the vertical resolution of the T41 I and T53 retrievals is indicated by the spacing of the plot symbols.

the light curves shown in Fig. 9. It is interesting to note that the minima and maxima in the T41 I and T53 profiles are out of phase, particularly between 500 and 600 km. The T41 I densities are approximately two times higher than the T53 densities above 850 km. These results indicate that the density profiles can vary substantially between different observations, and this variability makes it difficult to compare different retrievals with each other and photochemical models objectively. More data are required to establish the nature and magnitude of the typical variations.

Fig. 24 shows the density profiles of C_2H_4 based on T41 I and T53 data, Voyager UVS data (Vervack et al., 2004) and preliminary UVIS results for flyby Tb (Shemansky et al., 2005). Qualitatively, the T41 I and T53 density profiles are similar to the density profiles of C_2H_2 presented above for the same flybys in that the profiles contain large perturbations that coincide with the extinction layers in the light curves. The difference between the T41 I and T53 densities of C_2H_4 above 800 km is also similar to the difference in the densities of C_2H_2 between these two flybys. The UVS densities

agree roughly with the mean density implied by the T41 I and T53 profiles below 850 km but lack the strong perturbations seen in the UVIS data. This is curious because the UVS light curves contained a two-layer structure similar to what we observe (Broadfoot et al., 1981) and thus the lack of structure in the Vervack et al. (2004) profile could be related to uncertainties in the retrieval. The UVIS Tb II density agrees with the UVS density above 900 km, but both the UVS and Tb II results disagree with our retrieval. We note that the slope in both the UVS and Tb II results appears too shallow and thus the T41 I and T53 densities are probably more reliable than the UVS or Tb II results.

Fig. 25 shows the density profiles for C_4H_2 , C_6H_6 , HCN , and HC_3N derived from the T41 I and T53 occultations. The vertical resolution of the inverted density profiles is indicated by the spacing of the plot symbols. Again, the density profiles contain perturbations that coincide with the layers in the light curves. These perturbations in the column density profiles are occasionally so sharp that we had to degrade the altitude resolution severely to ~ 50 km for some of

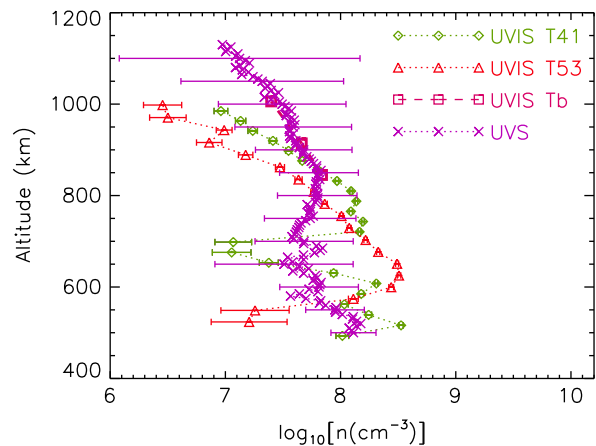


Fig. 24. Density profile of C_2H_4 based on different observations. The UVIS Tb densities are based on the occultation of λ Sco analyzed by Shemansky et al. (2005). The UVS ingress densities are from Vervack et al. (2004). Note that the vertical resolution of the T41 I and T53 retrievals is indicated by the spacing of the plot symbols.

the species in order to avoid negative densities near the minimum in the T41 I data. For the same reason we have not plotted densities for T53 below 550 km. It should be noted that these problems associated with the inversion method do not imply that the results are inaccurate. The data simulation in Section 2.3 shows clearly that the inversion is accurate at some resolution even when large perturbations are present in the data.

Finally, we compared our results for the photochemically active species with CIRS measurements below 500 km and INMS measurements in the thermosphere. This comparison is best done in terms of mixing ratios. However, stellar occultations at FUV wavelengths cannot be used to derive the density of N_2 , which absorbs primarily in the EUV. Instead, we used the N_2 densities measured by HASI (Fulchignoni et al., 2005) to calculate volume mixing ratios. In order to remove the wave-like features from the HASI data, we fitted the density profile with a simple slope, assuming that density decreases exponentially with altitude. We then calculated the UVIS mixing ratios based on the T41 I data and the smooth version of the HASI density profile. The results are shown in Fig. 26, together with mixing ratios measured by INMS and CIRS. We note that using the HASI density profile can lead to potentially large systematic errors in the UVIS mixing ratios, particularly if the temperature profile differs significantly from the HASI measurements. Because the T53 temperatures are generally cooler than the T41 I or the HASI measurements (see Section 4.1), we did not include mixing ratios for T53 in Fig. 26.

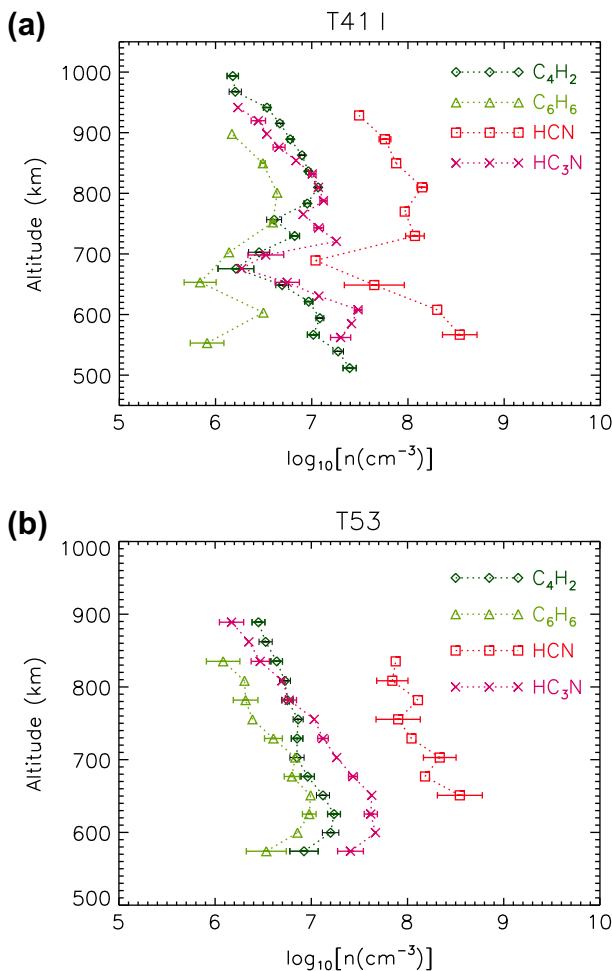


Fig. 25. Density profiles of minor species based on the T41 I and T53 occultations.

The CIRS mixing ratios were taken from Vinatier et al. (2010a). They are based on observations during flyby T27 (March, 2007) that probe latitudes near 20°S. We chose this location for comparison because it is close to the latitude of the T41 I observations in the southern hemisphere. The CIRS limb measurements of the abundances of C_2H_2 and HCN extend to altitudes above 400 km and connect with the UVIS measurements. The CIRS mixing ratios of HCN are in good agreement with the altitude dependence implied by the UVIS measurements. The same applies to C_2H_2 , although there is a slight disagreement between the CIRS and UVIS profiles near 450 km. This could be due to uncertainties in the background density profiles and/or retrieval of the UVIS density profiles near the lower altitude limit of the light curves. There are no CIRS measurements for C_4H_2 , C_2H_4 , and HC_3N in the upper stratosphere and mesosphere. Broadly speaking, the UVIS results are in agreement with the general trend implied by the INMS and CIRS measurements, i.e., that the mixing ratios of the higher order hydrocarbon and nitrile species increase steadily with altitude as these species diffuse down to the stratosphere from the

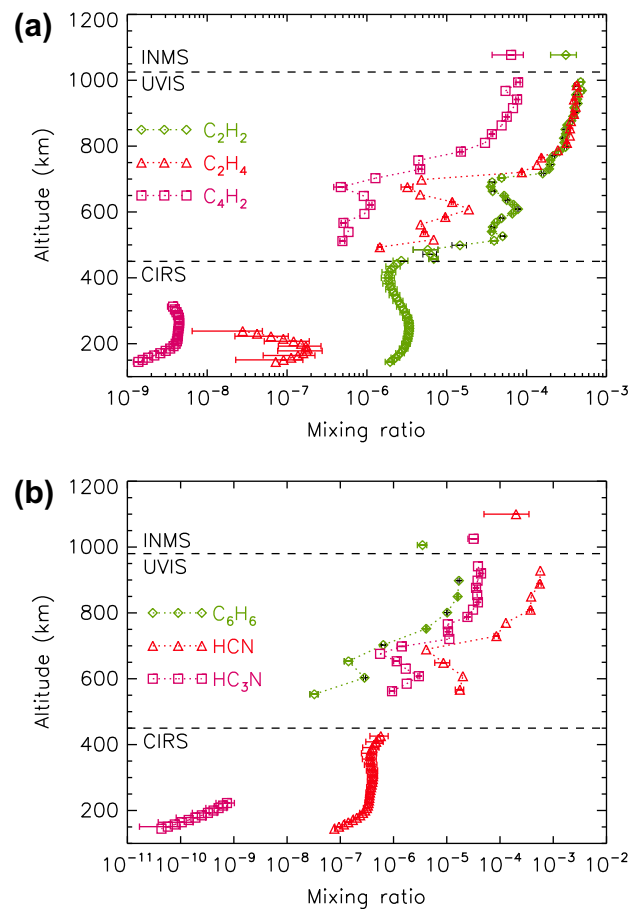


Fig. 26. Volume mixing ratios for various minor species. The INMS mixing ratios for C_2H_2/C_2H_4 , C_4H_2 , and HC_3N are globally averaged values that were corrected for the effects of wall adsorption/desorption within the instrument (see Table 4 in Cui et al., 2009). The INMS mixing ratios for HCN and C_6H_6 were taken from Vuitton et al. (2007, 2008). The mixing ratio for HCN is based on data from flyby T5 at 74°N while the mixing ratio of C_6H_6 was measured during flyby T26 at 25.7°N. The latter value was not corrected for the effects of chemistry that takes place on the chamber walls in the instrument. The CIRS mixing ratios were taken from Vinatier et al. (2010a) and they were measured during flyby T27 near 20°S. The UVIS mixing ratios are based on the T41 I data and were calculated with the density profile measured by HASI (Fulchignoni et al., 2005). As we did not account for uncertainties in the HASI profile, or systematic uncertainty arising from a possible departure of the real density profile from the HASI measurements, the true error of the UVIS mixing ratios is likely to be larger than that implied by the figure.

photochemical production region in the mesosphere and lower thermosphere. Taken together, the UVIS and CIRS data imply a presence of a minimum near 400 km in the mixing ratios of C_2H_2 , C_2H_4 , and C_4H_2 . However, it should be noted here that the T41 I results do not coincide exactly with the T27 CIRS measurements in terms of location and time.

The INMS mixing ratios for the mixture of C_2H_2/C_2H_4 , C_4H_2 and HC_3N were retrieved by Cui et al. (2009). These are globally averaged values that were properly corrected for the wall adsorption and desorption effects within the INMS Closed Source Neutral (CSN) mode. They are in very good agreement with the UVIS data and support the conclusion that, as expected, the photochemical production region of these species is indeed located in the thermosphere. The INMS mixing ratios for HCN and C_6H_6 are based on Vuitton et al. (2007, 2008). The abundance of HCN was not determined directly – rather it is based on the inferred abundance of $HCNH^+$ in the INMS measurements and reversing the chemistry that leads to the production of this ion. The estimated mixing ratio is consistent with the UVIS results and implies that the mixing ratio of HCN decreases with altitude above 1000 km. There is a gap between the UVIS and INMS measurements of the abundance of C_6H_6 between 850 and 1000 km, but the comparison implies that the mixing ratio of C_6H_6 also decreases with altitude above 850 km. We note, however, that we used the uncorrected INMS abundance C_6H_6 in Fig. 26 and in reality the given value is more likely to reflect the combined abundance of C_6H_6 and C_6H_5 . The INMS mixing ratios of HCN and C_6H_6 were measured during flybys T5 and T26, respectively, probing latitudes of 74° and 25.7° . Thus variations with latitude and time are also possible.

The broad agreement between our measurements and other Cassini data provide confidence that we have correctly identified the important absorbers in the data. Once additional UVIS data are analyzed, a more thorough comparison between models and existing observations should solidify this conclusion. We note that a comparison of the CIRS and INMS data with the UVIS results allows for density profiles to be characterized from the photochemical production region in the thermosphere to lower stratosphere at different locations and times. The results will provide valuable constraints on the chemistry and dynamics in the atmosphere of Titan.

3.4. Aerosols

In Section 3.1 we argued that both gaseous absorbers and aerosols are required to explain the appearance of the extinction layers in the light curves. The first part of this claim was verified in Sections 3.2 and 3.3. In the former we showed that the average transmission spectra within the extinction layers of the T41 I data were best fitted with a combination of minor species and aerosols. In the latter, we verified that the extinction layers coincide with peaks in the density profiles of the gaseous species. This is nicely illustrated by Fig. 8 that shows the optical depth contours for T41 I and T53. The contours indicate that the strong absorption lines of C_2H_2 , C_4H_2 and C_2H_4 are enhanced within the layers. To complete the argument, we now show that the extinction profiles of the aerosols also contain layers. In particular, the detached haze layer appears consistently in the data between $z = 450$ – 550 km whereas the higher altitude layers in T41 I, T53, and similar occultations are mostly due to gaseous absorbers.

Fig. 27 shows optical depth of the aerosols as a function of impact parameter for the T41 I and T53 occultations. In order to retrieve optical depth due to aerosols, we assumed that the aerosols are spherical with a radius of $r_a = 12.5$ nm at all altitudes and used Mie theory to obtain extinction cross sections assuming the optical properties of tholins (Khare et al., 1984). We note, however, that the choice of a radius merely fixes the wavelength

dependency of the aerosol cross sections. This dependency does not vary significantly with the size of the particles (see below) and thus the optical depth profiles can be used to derive density profiles for aerosols of different size – as long as the aerosols have the optical properties of spherical tholins. We chose this method of obtaining the optical depth profiles because it allows us to include aerosols in the LM fits. This means that we do not have to assume that a specific wavelength range is entirely free from absorption by other species and we can use the full wavelength range of the FUV channel to constrain the extinction coefficients of the aerosols.

In order to find out if the UVIS data could be used to constrain the size of the aerosols by exploring the wavelength dependency of aerosol extinction, we used the refractive indices of the Khare et al. (1984) tholins to calculate extinction cross sections for spherical aerosols with radii between $r_a = 0.2$ – 60 nm. The average cross section of these aerosols at wavelengths between $\lambda_p = 1850$ – 1900 Å increases by eight orders of magnitude from 3.4×10^{-22} cm² to 3.1×10^{-14} cm² with increasing radius. We fitted the cross sections with a wavelength dependency proportional to $\lambda^{-\alpha}$ at wavelengths between 1400 and 1900 Å. We found that α increases from ~ 1.4 to 2.3 as r_a increases from 0.2 to 25 nm. As the radii grow larger than 25 nm, α decreases and for $r_a = 60$ nm, $\alpha = 0.6$. We showed in Section 3.2 that the UVIS data are consistent at all altitudes with $\alpha < 2.5$. Unfortunately this constraint includes all possible particle radii. Thus the size of the aerosols cannot be constrained further without observations of aerosol extinction and scattering at other wavelengths.

We inverted the optical depth profiles of the aerosols in order to obtain local extinction coefficients. Fig. 28 shows the resulting profiles for T41 I and T53. Aerosol extinction in the T41 I data peaks in the detached haze layer near 520 km and tentatively, there is another peak near 800 km. In the T53 data, aerosol extinction peaks near 470 km and tentatively, there is another peak near 600 km. We note that there is a small altitude shift between the peaks observed in the local extinction profiles and the optical depth profiles. This is because the optical depth profiles represent column integrated extinction, which should be compared with the ISS images rather than local extinction. Thus the location of the detached haze layer at $a = 450$ km in the T53 data is consistent with the collapse of the layer that began a few months prior to the equinox (West et al., 2011). This completes the argument that the lower altitude extinction layers in the UVIS data are associated with the detached haze layer while the higher altitude extinction layers are mostly due to perturbations in the density profiles of the gaseous species.

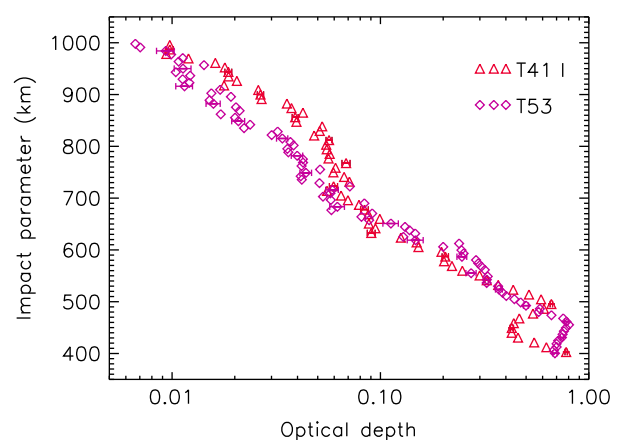


Fig. 27. Optical depth profiles of aerosols derived from the T41 I and T53 occultations. Here the optical depth was averaged over wavelengths between 1850 and 1900 Å (see text for the details of the retrieval).

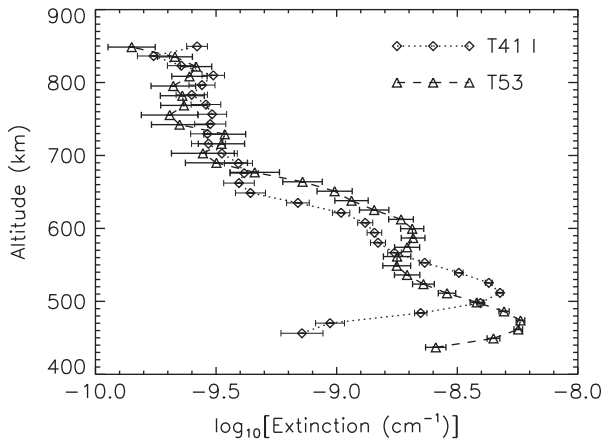


Fig. 28. Extinction due to aerosols averaged between 1850 and 1900 Å as a function of altitude for T41 I and T53.

Lavvas et al. (2009) used Cassini/ISS images (Porco et al., 2005) and aerosol extinction coefficients derived from the λ Sco (Tb II) occultation (Liang et al., 2007) to constrain the imaginary part k of the refractive index and the radius of the aerosols. They found that the aerosols in the detached haze layer have a radius of $r_a = 40$ nm and $k < 0.3$ at 1875 Å. These results are based on the assumption that aerosols are the only absorber responsible for extinction at wavelengths between 1850 and 1900 Å in the UVIS data. Fig. 16 and related discussion indicate that this assumption is safe within the detached haze layer but it could be dangerous at higher altitudes. The presence of additional absorbers lowers aerosol extinction and allows for larger particle sizes. Assuming a radius of $r_a = 40$ nm, the number density of the aerosols in the detached haze layer derived from the extinction coefficients is ~ 40 cm $^{-3}$ for T41 I, and ~ 70 cm $^{-3}$ for T53. These densities are comparable to each other and slightly higher than those obtained for Tb II. Unfortunately, the ISS images cannot be used to constrain the size of the high altitude aerosols because the images only extend to 600 km in altitude. We used other constraints to obtain limits for their size. The results are discussed in Section 4.4.

4. Discussion

In previous sections of the paper we discussed the methods and results of the data analysis. In this section we discuss the implications of the retrieved density profiles on the structure of the atmosphere.

4.1. Temperature profiles

Assuming that CH $_4$ is uniformly mixed with N $_2$, we used the density profiles of CH $_4$ to derive temperature profiles for T41 I and T53 at altitudes between 600 and 1100 km. These profiles are shown in Fig. 29 together with the HASI measurements (Fulchignoni et al., 2005). The T41 I and T53 temperatures are similar at altitudes below 780 km, and slightly cooler than the HASI temperatures. The T41 I temperature agrees fairly well with the HASI measurements between 800 and 1100 km, whereas the T53 temperature is unrealistically high above 900 km and significantly cooler than the other measurements between 780 and 900 km. We note that the CH $_4$ temperature profiles presented here are only accurate below the homopause. Above the homopause, CH $_4$ is diffusively separated and the derived temperatures are anomalously high. The agreement of the T41 I temperature with the HASI measurements at high altitudes therefore implies that the CH $_4$ homo-

pause is located between 1000 and 1100 km. However, the steep increase in temperature with altitude in the T53 data indicates that CH $_4$ is diffusively separated above 900 km. This raises the interesting possibility that the altitude of the apparent homopause on Titan varies with latitude and/or time.

The altitude of the homopause coincides with a distinct change in the slope of the density profile of CH $_4$. The T53 density of CH $_4$ (see Fig. 22) decreases with a scale height of $H_\rho = 50$ km up to ~ 900 km. This value is consistent with a mean temperature of $T \sim 150$ K below 750 km. Because gravity decreases with altitude, the measured scale height is also consistent with a lower mean temperature between 750 and 900 km. Above 900 km the T53 density of CH $_4$ decreases with a scale height of $H_\rho = 97$ km. Given that the mass ratio of N $_2$ to CH $_4$ is 1.8, this value is roughly consistent with diffusive separation above 900 km with a mean temperature of $T = 150$ K, which is in line with the mean temperature of the thermosphere determined from the INMS measurements (Cui et al., 2009). The altitude of the homopause in the T53 data is also consistent with the results of Yelle et al. (2008) who used the density profile of ^{40}Ar measured by the INMS to derive an eddy diffusion coefficient of $K_{zz} \sim 3 \times 10^7$ cm 2 s $^{-1}$ in the lower thermosphere that implies a homopause near 850 km.

The T41 I density profile of CH $_4$ (see Fig. 22) can be fitted with a scale height of $H_\rho = 55$ km below 850 km. This corresponds to a temperature of $T \sim 152$ K. Above 850 km, the density of CH $_4$ decreases with a scale height of $H_\rho = 78$ km. This change in the slope of the density profile can be interpreted in two different ways. With a mean temperature of $T \sim 150$ K it implies an intermediate regime between diffusive separation and mixing. Alternatively, with a mean temperature of 180–200 K that agrees with the HASI measurements, it implies that CH $_4$ is uniformly mixed up to the altitude of 1000–1100 km. The latter result agrees with earlier Voyager measurements (Strobel et al., 1992; Vervack et al., 2004) and INMS measurements (e.g., Yelle et al., 2008; Cui et al., 2009) that are consistent with a high CH $_4$ homopause. As we pointed out above, the differences in the density profiles of CH $_4$ between T41 I and T53 may imply that the apparent altitude of the CH $_4$ homopause changes with time and/or latitude. This could be due to changes in global circulation or atmospheric escape. We discuss these possibilities further below.

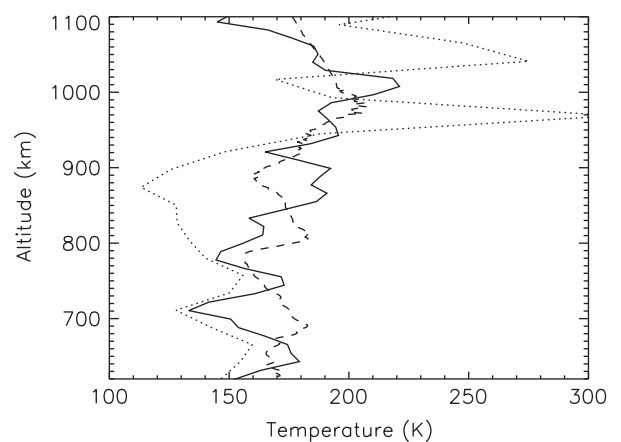


Fig. 29. Temperature profiles derived from the density profiles of CH $_4$ for T41 I (solid line) and T53 (dotted line). The altitude resolution is 20–40 km, with the higher resolution obtained for T41 I. The dashed line shows the HASI temperature profile (Fulchignoni et al., 2005). The temperature profiles show evidence for waves with a vertical wavelength of 100–200 km and an amplitude of 10–20 K. The T41 I profile agrees well with the HASI profile above 800 km, although with a variable wave pattern. The T53 temperatures are unrealistically high above 900 km due to diffusive separation of CH $_4$.

While K_{zz} is normally associated with turbulent mixing and breaking waves, it is also well known that vertical bulk motion driven either by circulation or escape of an atmospheric constituent can have the same effect on the composition as an enhanced K_{zz} in one-dimensional models. By assuming a nominal eddy diffusion coefficient of $K_{zz} = 5 \times 10^7 \text{ cm}^2 \text{ s}^{-1}$, Muller-Wodarg et al. (2003) showed that while the nominal homopause is located near 800 km, the timescale for vertical and horizontal motion due to circulation is shorter than the timescale for molecular diffusion between 800 and 1200 km. Mixing of the atmosphere by circulation in this region can lead to an effective $K_{zz} \sim 10^9 \text{ cm}^2 \text{ s}^{-1}$ that shifts the homopause to a higher altitude in agreement with the observations.

The differences between the T41 I and T53 occultations could thus be due to mixing by large scale circulation. The T41 I occultation probed a region of the atmosphere near the subsolar latitude during night time whereas T53 probed northern midlatitudes during daytime. Asymmetric solar heating of the detached haze layer during daytime can lead to overturning meridional circulation that, possibly accompanied by strong zonal winds, leads to upwelling at subsolar latitudes and downwelling at higher and lower latitudes. Upwelling leads to more efficient mixing of the atmosphere, producing a higher CH_4 homopause, whereas downwelling leads to less efficient mixing of the heavier constituents. This is consistent with the differences between the T41 I and T53 occultations. The presence of strong circulation is also supported by the temperature difference between the occultations above 750 km. This temperature difference is consistent with INMS measurements indicating that the equatorial regions of the thermosphere are generally warmer than the polar or mid-to-high latitude regions (Cui et al., 2009).

Mixing by circulation should affect all of the species whereas escape is more effective in changing the density profiles of the lighter species. Yelle et al. (2008) showed that argon is not effectively mixed above the homopause near 850 km while CH_4 and H_2 are. They pointed out that the density profile of CH_4 measured by the INMS is consistent with a diffusion-limited escape flux of $2.5\text{--}3.0 \times 10^9 \text{ cm}^{-2} \text{ s}^{-1}$. Similarly, the density profile of H_2 in the upper atmosphere can be explained by an escape flux of $1.4 \times 10^{10} \text{ cm}^{-2} \text{ s}^{-1}$ (Cui et al., 2008). Both of these fluxes are significantly higher than the thermal Jeans escape rate. We note that a simultaneous analysis of the density profiles of several minor species could be used to distinguish the roles of circulation and escape mechanisms in shaping the density profiles of CH_4 and H_2 more accurately. However, such analysis requires more observations that cover a much larger sample of latitudes and local times than the present study.

All three temperature profiles in Fig. 29 show evidence for wave-like variations with an amplitude of 10–20 K and a vertical wavelength of 100–200 km. This is not surprising – evidence for similar waves has been obtained by the HASI instrument throughout the atmosphere (Fulchignoni et al., 2005) and INMS in the thermosphere (Muller-Wodarg et al., 2006). Evidence for waves was also seen in the Voyager data (e.g. Hinson and Tyler, 1983; Friedson, 1994) and ground-based stellar occultations (e.g., Sicardy et al., 1999). Strobel (2006) suggested that the perturbations observed in the upper atmosphere could be caused by gravitational tidal waves, which are driven by the small but finite eccentricity of Titan's orbit around Saturn. These waves are expected to saturate near 500 km. Once evanescent, their amplitude no longer grows with altitude and they become quasi-sinusoidal, i.e., similar in appearance to the waves in the HASI data. The saturation amplitude and vertical wavelength of these waves depend strongly on the background zonal wind profile.

In order to explore the nature of the temperature perturbations, we fitted the T41 I temperature profile with slopes of dT/dz

$\sim 0.17 \text{ K km}^{-1}$ between 650 and 870 km and $dT/dz \sim 0.13 \text{ K km}^{-1}$ between 870 and 1000 km. We then subtracted these slopes from the retrieved temperature profile in order to isolate the perturbations, which are shown in Fig. 30. The perturbations have an amplitude of 10–20 K and a vertical wavelength of 80–200 km, although they probably represent a superposition of several different waves and therefore the results should be interpreted with caution. Nevertheless, the properties of the waves are broadly consistent with the amplitude and wavelength of tidal gravity waves (e.g., Strobel, 2006). Unfortunately, the uncertainties related to the retrieval and the limited altitude range of the data do not justify more extensive fits to characterize the waves. More observations are required for such an analysis. We also investigated the possibility that the sharp temperature gradients associated with the wave are superadiabatic and drive local convective instabilities (e.g., Fulchignoni et al., 2005). Fig. 31 shows the temperature gradients for T41 I evaluated from the data together with the adiabatic lapse rate. It indicates that the temperature gradients can become slightly superadiabatic. This could be produced by breaking gravity waves.

4.2. Chemical and transport timescales

Before characterizing the density profiles of the minor species in detail, it is instructive to explore the timescales for different physical processes that control the composition of the atmosphere. The continuity equation for individual species s is given by:

$$\frac{\partial \rho_s}{\partial t} + \nabla \cdot (\rho_s \mathbf{v}) = -\frac{1}{r^2} \frac{\partial}{\partial r} [r^2 (F_D + F_{zz})] + (P_s - L_s) \quad (12)$$

where F_D and F_{zz} are mass fluxes due to molecular and eddy diffusion, respectively, and P_s and L_s are chemical production and loss rates, respectively. Diffusive fluxes occur predominantly in the vertical direction and thus horizontal diffusion is neglected. The second term on the left hand side of Eq. (12) describes advection due to horizontal and vertical winds. Under the assumption of hydrostatic equilibrium vertical winds are driven exclusively by diverging or converging horizontal flows to ensure the conservation of mass by circulation. Although vertical winds are much slower than horizontal winds, they can have a large impact on the density profiles of different species because the scale height of the atmosphere is typically much shorter than the relevant horizontal length scale that is often estimated by $L \sim R_p$ where R_p is the radius of the planet.

Table 4 presents the timescales for advection, diffusion and photochemical loss processes at representative altitudes in Titan's mesosphere and lower thermosphere. We defined the chemical time constant as $\tau_c = (L_s/\rho_s)^{-1}$ and calculated it by using the density

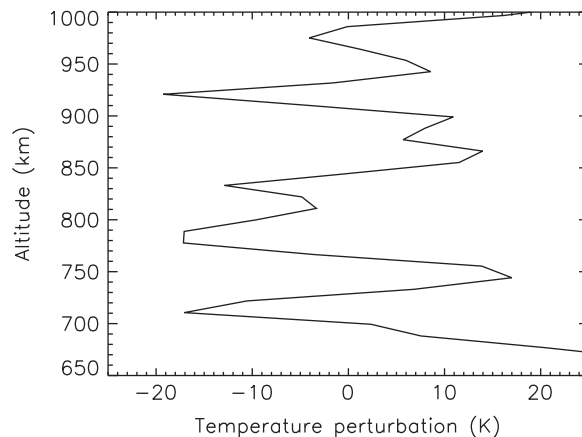


Fig. 30. Temperature perturbation derived from the T41 I CH_4 temperature profile.

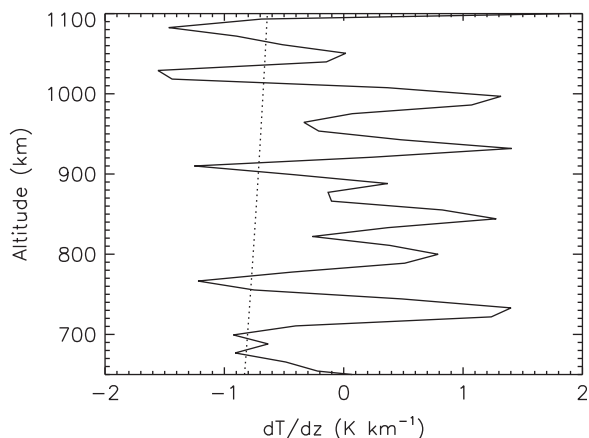


Fig. 31. Temperature gradients based on the T41 I data (solid line). The dotted line shows the adiabatic lapse rate $\Gamma = -g/C_p$.

profiles and reaction rate coefficients included in the model of Lavvas et al. (2008a,b). The timescale for molecular diffusion is given by $\tau_D = H^2/D_{st}$ where H is the scale height. We calculated these timescales for different constituents by using binary diffusion coefficients of the relevant species with N_2 . In order to calculate the eddy diffusion timescale (τ_{zz}), we used K_{zz} derived by Yelle et al. (2008). The transport timescales for horizontal (τ_U) and vertical winds (τ_w) were calculated by Muller-Wodarg et al. (2003). We note that these timescales may be too long between 500 and 900 km. If the wind speeds in the mesosphere are comparable to stratospheric wind speeds (e.g., Flasar et al., 2005), the horizontal transport timescale can be comparable to the timescale for turbulent mixing.

As expected, the parameters in Table 4 place the homopause near 850 km. The eddy diffusion timescale is shorter or comparable to the advection timescale below the homopause. This gives rise to the diffusion of the higher order hydrocarbon and nitrile species from the photochemical production region near 800 km down to the stratosphere. We note that this picture can be slightly modified by upwelling and subsidence associated with circulation that can cause latitudinal variations in the mixing ratios of the constituents similar to those observed in the stratosphere (e.g., Coustenis et al., 2010). The chemical time constants below 850 km are generally longer than the diffusion timescale for species such as C_2H_2 , C_2H_4 , HCN and HC_3N . However, for C_6H_6 and C_4H_2 the chemical time constants are shorter than the prominent transport timescales and thus their density profiles could be closer to chemical equilibrium in the mesosphere than the density profiles of the other species detected in the UVIS data.

The chemical timescales for C_2H_2 and C_2H_4 at 1000 km are longer than the timescale for molecular diffusion. In principle, the density profiles of these species can thus be used to determine whether the atmosphere really is uniformly mixed at high altitudes in the T41 I data or not. However, a closer examination of the timescales indicates that this is not safe. The difference between the chemical and diffusion timescales is not necessarily sufficient, especially if one accounts for the larger scale height associated with higher temperatures between 800 and 1000 km.

Table 4
Chemical and transport timescales.

Altitude (km)	C_2H_2 , τ_c	C_2H_4 , τ_c	C_4H_2 , τ_c	C_6H_6 , τ_c	HCN, τ_c	HC_3N , τ_c	τ_D	τ_{zz}	τ_w	τ_U
500	2×10^7	6×10^6	2×10^5	2×10^5	2×10^9	10^7	5×10^8	10^6	4×10^8	4×10^8
750	6×10^6	3×10^6	5×10^5	2×10^5	10^7	10^7	6×10^6	10^6	4×10^6	4×10^6
1000	10^6	10^6	2×10^5	10^5	10^6	3×10^5	10^5	10^6	4×10^5	4×10^5

The values are given in seconds for $T = 160$ K and $H = 55$ km. The diurnal time constant is $\sim 2 \times 10^5$ s.

More complex modeling of the chemistry and dynamics and comparison with data may enable this type of analysis in the future. For reference, the scale heights derived from the T41 I density profiles of C_2H_2 and C_2H_4 above 850 km are 76 km and 61 km, respectively. The large difference between these values indicates that at least the density profile of C_2H_4 is affected by photochemical processes above the homopause.

4.3. Density structure

The temperature profiles in Fig. 29 indicate that the density profile of CH_4 is perturbed by waves. The amplitude of the perturbations is similar to the saturation amplitude of tidal gravity waves in the mesosphere (Strobel, 2006). However, compared to CH_4 the perturbations in the density profiles of the other minor species are much larger. Initially, it would seem reasonable to argue that such large density perturbations cannot be caused by the same waves that are responsible for the temperature perturbations. We show below that this is not true and demonstrate that low frequency waves can cause large perturbations in the density profiles of the minor species as long as the mixing ratios of these species increase with altitude and the eddy diffusion coefficient is sufficiently low. In order to illustrate this argument, we focus our attention on the density profile of C_2H_2 based on the T41 I data and then briefly generalize our results to the other species. A more comprehensive analysis of the photochemical processes and dynamics is reserved for future work.

The density perturbation $\rho'(r)$ due to gravity waves is related to the pressure and temperature perturbations simply by the ideal gas law:

$$\frac{\rho'(r)}{\rho_0(r)} = \frac{p'(r)}{p_0(r)} - \frac{T'(r)}{T_0(r)} \quad (13)$$

where subscript 0 refers to the background (mean) fields in the atmosphere. The pressure perturbations are typically small, indicating that in general $\rho'(r)/\rho_0(r) \approx -T'(r)/T_0(r)$. The density perturbation $\rho'(r)$ and the mean density $\rho_0(r)$ are given by separate sums over the perturbations and densities, respectively, of the individual species. Thus the relative perturbations ρ'_s/ρ_{s0} of the constituents in Eq. (13) cannot be separated. Further, even if the density perturbation ρ'_s is comparable to the actual density of species s , the contribution of the species to the left hand side of Eq. (13) is at most comparable to its mass mixing ratios. Because the mass mixing ratios of the minor species other than CH_4 are negligible, Eq. (13) alone does not constrain the amplitudes of the relative perturbations ρ'_s/ρ_{s0} .

We note that in terms of the mass mixing ratios q_s , Eq. (12) can be written as (e.g., Jacobson, 1999):

$$\frac{\partial q_s}{\partial t} + (\mathbf{v} \cdot \nabla) q_s = \frac{1}{\rho} (P_s - L_s) + \frac{1}{\rho} \nabla \cdot (\rho K_{zz} \nabla) q_s \quad (14)$$

where K_{zz} is the eddy diffusion coefficient and we ignored molecular diffusion to simplify the equation. This is not a significant omission at this point, especially because most of the discussion in this section concerns the density profiles below the homopause. First, we analyzed the photochemical production and loss rates in the above equation. Fig. 32 shows the volume mixing ratio of C_2H_2 together

with mixing ratios calculated by the photochemical model of Lavvas et al. (2008a,b). Again, we used the smooth version of the HASI density profile (Fulchignoni et al., 2005) to calculate the mixing ratios from the data (see Section 3.3). The photochemical calculations are appropriate for the solar activity and latitude of the T41 I observations. Apart from the perturbations, the photochemical model is in reasonable agreement with the data.

The production of C_2H_2 above 500 km in the model is mostly due to photolysis of C_2H_4 . The photolysis rates peak near 800 km and once produced, C_2H_2 diffuses to lower altitudes where it is also partly destroyed by photolysis. As a result, the mixing ratio of C_2H_2 increases steeply with altitude between 500 and 800 km. Qualitatively, this scheme agrees with the results of Wilson and Atreya (2004) but disagrees with the results of Yung et al. (1984) who argued that reactions between the CH_2 radicals are the most important production mechanism of C_2H_2 in the upper atmosphere. We note that this simple scheme leads to a good qualitative agreement between the mean state mixing ratio of C_2H_2 in the UVIS data and photochemical models. This resolves the earlier problems associated with fitting the density profile of C_2H_2 derived from the Voyager/UVS data (Vervack et al., 2004) with photochemical models.

In order to assess the magnitude of the perturbations in the mixing ratio of C_2H_2 , we subtracted the model mixing ratios from the data. The resulting relative mixing ratio perturbations q'_s/q_{s0} as a function of altitude are shown in Fig. 33. The data were smoothed to an approximate vertical resolution of ~ 25 km before subtraction. The amplitude of the perturbations decreases with altitude. Below 750 km the large perturbations have an amplitude of ~ 40 –60%. We note that these results are uncertain because of uncertainties in the retrieval and because the mean mixing ratios are not known exactly. Also, we did not take into account the fact that the density of the atmosphere is also perturbed. If, for instance, the total density perturbations are in phase with the minor species density perturbations, the mixing ratio perturbations would appear smaller. It is not straightforward to determine the vertical wavelength of the perturbations because the observed pattern could be due to several, superimposed waves of different origins. However, the large perturbations appear to have a wavelength of 150–200 km.

In order to show that large perturbations driven by low frequency waves are possible, we derived a simple expression for the amplitude of the relative mixing ratio perturbations based on the equation of continuity for q_s by assuming linear perturbations. The details of the derivation and the assumptions leading to the

result are included in Appendix A. Basically, we assumed that the perturbations are waves and expressed them as:

$$q'_s = q_{s1} \exp[i(mr + k\phi - \omega t + \theta_q)] \quad (15)$$

$$w' = w_1 \exp[i(mr + k\phi - \omega t + \theta_w)] \quad (16)$$

$$\rho' = \rho_1 \exp[i(mr + k\phi - \omega t + \theta_\rho)] \quad (17)$$

where ω is the frequency, m is the vertical wavenumber, k is the zonal wavenumber, and $\theta_w = \theta_\rho + \pi/2$, θ_ρ , and θ_q are the phase angles of w' and ρ' and q'_s , respectively. We treated w' and ρ' as free parameters and did not seek a self-consistent solution for these quantities. Therefore we had to fix the phase relationship between w' and ρ' to something that is consistent with, for instance, the results of Strobel (2006) for gravitational tidal waves. Further, we assumed that the amplitudes of the perturbations are constant in altitude. This assumption is not generally valid but it is reasonable in regions where the waves become saturated and their amplitudes no longer grow with altitude. These assumptions are somewhat *ad hoc*, but they are satisfactory for our purposes. Our aim is merely to demonstrate that certain types of waves can cause large perturbations in the density profiles of the minor species. A more quantitative characterization of the physical nature and origin of such waves should be pursued in future work.

Substitution of the perturbations given above into the equation of continuity (A.1), considerable algebra and several simplifications yield an expression for the relative amplitude $r_{s1} = q_{s1}/q_{s0}$ of the mixing ratio perturbations:

$$r_{s1} \exp(i\theta_q) = \frac{1}{q_{s0}} \frac{\partial q_{s0}}{\partial r} \frac{[(w_1/m) + (\rho_1/\rho_0)K_{zz}] \exp(i\theta)}{\sqrt{[(\Omega/m) - w_0 - (K_{zz}/H)]^2 + m^2 K_{zz}^2}} \quad (18)$$

$$\theta = \theta_\rho + \pi - \tan^{-1} \left[\frac{mK_{zz}}{(\Omega/m) - w_0 - (K_{zz}/H)} \right] \quad (19)$$

where H is the scale height, q_{s0} is the unperturbed mass mixing ratio, and $\Omega = \omega - ku_0/(r \sin \theta)$ is the intrinsic Doppler-shifted wave frequency. Note that we assumed that the phase of the waves propagates eastward towards lower altitudes so that $m < 0$ and $k > 0$.

At the 'wave advection' limit where $K_{zz} \rightarrow 0$, the relative amplitude r_{s1} is given by:

$$r_{s1} = \left| \frac{w_1}{m} \left(\frac{\Omega}{m} - w_0 \right)^{-1} \frac{1}{q_{s0}} \frac{\partial q_{s0}}{\partial r} \right| \quad (20)$$

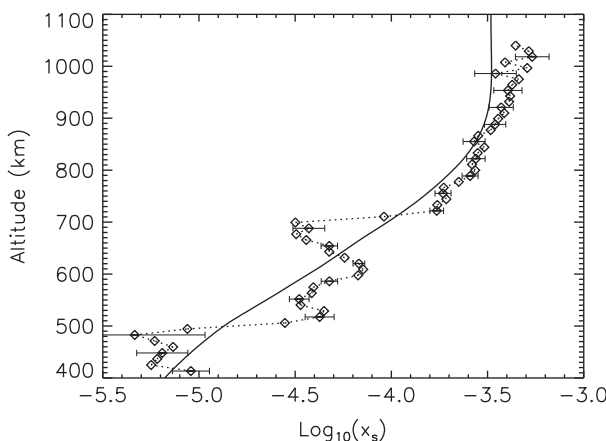


Fig. 32. The volume mixing ratio x_s of C_2H_2 derived from the T41 I data (diamonds) and based on the photochemical model of Lavvas et al. (2008a) (solid line). Note that the volume mixing ratio was calculated by using the HASI density profile (see text).

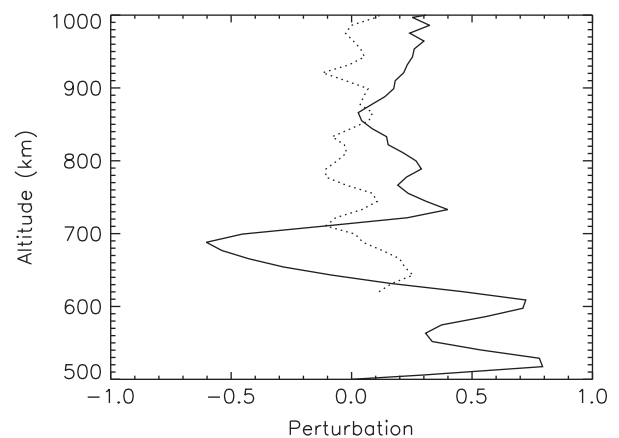


Fig. 33. The relative C_2H_2 mixing ratio perturbation q_{s1}/q_{s0} (solid line) and the CH_4 temperature perturbation (dotted line) normalized with a mean temperature of 160 K. Note that the results are uncertain because of the uncertainties of the retrieval and because the mean state is not known *a priori*.

These simple expressions clarify the physical insight into the mechanism that leads to large perturbations. In regions where the gradient of the mixing ratio for C_2H_2 is positive, i.e., below ~ 800 km in Titan's atmosphere, the perturbations in the mixing ratios are in phase with the temperature perturbations and 90° out of phase with the velocity perturbations. The sink that causes the minimum near 680 km arises because the wave-related velocity perturbation is positive above the minimum and therefore the wave advection term in Eq. (A.2) is positive. However, this mechanism is only effective if the frequency of the wave is sufficiently slow. Otherwise advection does not have enough time to establish large fluctuations before the velocity perturbation changes. Also, when $K_{zz} \neq 0$, eddy diffusion acts to remove any density perturbations. At sufficiently high values of K_{zz} , the phase of the mixing ratio perturbations changes and the amplitude of the perturbations becomes small.

We estimated the required values for w_1 , m , Ω , and w_0 that would lead to the observed value of $r_{s1} \sim 0.4$ – 0.5 for C_2H_2 . For this purpose, it is convenient to define a frequency parameter given by:

$$\Omega_l = \left| m \left(\frac{\Omega}{m} - w_0 \right) \right|$$

At the limit where $w_0 = 0$ and $u_0 = 0$, this parameter is simply $\Omega_l = \omega$. According to photochemical calculations, the gradient term for C_2H_2 near 680 km is $(1/q_{s0})\partial q_{s0}/\partial r \sim 10^{-5} \text{ m}^{-1}$. At the limit of zero background flow, a ratio of $w_1/\omega \sim 4.4 \times 10^4 \text{ m}$ therefore leads to the required 40–50% perturbation in the mixing ratio of C_2H_2 near the minimum of 680 km. Because of the large w_1/ω ratio, low frequency waves are required to cause the observed perturbations. If we assume that the period of the observed waves is equal to one Titan rotation, i.e., $\omega = 4.5 \times 10^{-6} \text{ Hz}$, the required value for the amplitude of the vertical velocity perturbation is $w_1 = 20 \text{ cm s}^{-1}$. It is interesting to note that this value is consistent with the saturation amplitude for gravitational tidal waves, which also have the required frequency (Strobel, 2006). Alternatively, thermal tides could also have a similar, low frequency. We note that solar heating of the detached haze layer (Lavvas et al., 2009) could possibly excite such tides in the upper atmosphere of Titan. This possibility should be addressed in future studies.

The characteristics of gravitational tidal waves depend strongly on the background zonal wind profile. Strobel (2006) calculated the saturation amplitudes of the waves for three different zonal wind profiles: weak zonal winds, 'realistic' zonal winds and strong zonal winds. In the weak wind case the zonal wind speed was set to 135 m s^{-1} at 170 km. The realistic zonal wind case was based on the measured wind speeds of 183 m s^{-1} near 220 km (Moreno et al., 2005) and the strong zonal wind case included strong high altitude winds that may be required to explain the latitudinal density gradients in INMS observations (e.g., Muller-Wodarg et al., 2006). The zonal wind speeds above 600 km for the weak, realistic and strong wind cases were 45, 55, and 125 m s^{-1} , respectively. Assuming that the zonal wind speed is 55 m s^{-1} above 600 km, we obtain a Doppler-shifted frequency of $\Omega \sim 2.9 \times 10^{-5} \text{ Hz}$ for the semi-diurnal tide near the equator at 680 km. In this case, the required velocity perturbation is $w_1 \sim 130 \text{ cm s}^{-1}$, which is larger than the values calculated by Strobel (2006). We note, however, that the background dynamics above 500 km is uncertain, and there are many possible sources of gravity waves with different characteristics. Further, the frequency parameter Ω_l can be made comparable to ω above simply by introducing a finite (local) value for w_0 and/or by adjusting the assumed gradient of the mixing ratio. Given these uncertainties, we have demonstrated sufficiently that the observed perturbations can be caused by low frequency waves and our results therefore constitute evidence for the presence of such waves in the upper atmosphere of Titan.

The perturbations can also be damped by eddy diffusion. We used Eqs. (18) and (19) to estimate the limiting value of K_{zz} that allows for the perturbations to persist. At $K_{zz} = 10^7 \text{ cm}^2 \text{ s}^{-1}$, the relative perturbation amplitude reduces from $r_{s1} = 0.44$ to $r_{s1} = 0.42$ whereas for $K_{zz} = 10^8 \text{ cm}^2 \text{ s}^{-1}$, it reduces to $r_{s1} = 0.14$. With a nominal value of $K_{zz} = 3 \times 10^7 \text{ cm}^2 \text{ s}^{-1}$ (Yelle et al., 2008), the perturbation amplitude is $r_{s1} = 0.31$. A 44% perturbation in this case can be recovered if $w_1 \sim 30 \text{ cm s}^{-1}$. We note that the presence of the perturbations in the data places constraints on the possible values of K_{zz} . Even for relatively large values of $w_1 \sim 65 \text{ cm s}^{-1}$, K_{zz} must be lower than $\sim 10^8 \text{ cm}^2 \text{ s}^{-1}$.

Fig. 33 shows that the amplitude of the mixing ratio perturbations decreases with altitude and becomes very small above 850 km. There are two reasons for this behavior. First, the mixing ratio becomes nearly constant with altitude. Second, the timescale for molecular diffusion becomes shorter than the timescales for wave advection and eddy diffusion. Thus the wave is damped at high altitudes and the perturbations in the density profiles of the minor species become comparable to the relative temperature perturbations. We note that if the density perturbations are driven by waves, the amplitude of the perturbations depends on the gradient term $(1/q_{s0})\partial q_{s0}/\partial r$. We calculated the gradient terms for C_2H_4 , C_4H_2 , C_6H_6 , HCN and HC_3N near 680 km based on the photochemical model profiles. The values are 1.8×10^{-5} , 1.7×10^{-5} , 1.8×10^{-5} , 1.4×10^{-5} , and 1.5×10^{-5} , respectively. Thus the perturbation amplitudes for different species near 680 km in the T41 I data should be comparable, with C_2H_2 having a slightly shallower perturbation compared to the other species. The density profiles in Section 3.3 seem to confirm this trend, providing further support for the idea that the density perturbations really are waves. Obviously, the perturbations do not appear in the density profile of CH_4 because its mixing ratio is roughly constant with altitude. We note that the T41 I mixing ratios are in broad agreement with the photochemical model profiles with the exception of C_6H_6 . The model underestimates its mixing ratio by a factor of 5–10 above 800 km and overestimates the mixing ratio below 800 km. A more extensive comparison between photochemical models and the data is beyond the scope of this work and will be reserved for future work.

The linear perturbation model may not be appropriate for characterizing the large perturbations observed in the data. Therefore we used a numerical model to solve the continuity equation (14) with wave-like perturbations. We ignored chemical reaction terms and molecular diffusion, and forced the equation in the same way as the linear solution by introducing fixed perturbations to w and ρ . We separated the real and imaginary parts of the equation and integrated them iteratively over time by using a second order Runge–Kutta method with constant slope boundary conditions. The integration was carried out until the solutions reached steady state on a vertical grid extending from 300 to 1300 km with a cell spacing of 5 km. We looked for an agreement with the data by using the model mixing ratio of C_2H_2 as an initial condition. We adopted the eddy diffusion profile from Yelle et al. (2008) for the simulations.

Fig. 34 shows the model results contrasted with the observed density profile of C_2H_2 based on the T41 I data. It also shows the fixed perturbations assumed for the net density n , vertical velocity w and temperature T . The model provides a good fit to the data with a vertical wavelength of ~ 210 km and a vertical velocity perturbation of $w_1 = 35 \text{ cm s}^{-1}$. These parameters are roughly consistent with the linear calculations discussed above. We note, however, that the amplitude of the velocity perturbations and the vertical wavelength are obviously connected to the temperature and density perturbations, and their values cannot be chosen at random. Also, the vertical wavelength of the temperature perturbations appears to be shorter than 200 km and this implies that the density and temperature profiles could be affected by a superposition of several different waves. Clearly, our purpose here is not

to characterize these waves exactly but simply to demonstrate that large perturbations in the density profiles of the minor species caused by low frequency waves are possible.

Because the temperature and density perturbations may represent a superposition of several waves, trying to fit all of the features simultaneously could be misleading. Further, the large temperature perturbation observed in the HASI profile between 450 and 600 km may not be caused directly by the wave. Lavvas et al. (2009) demonstrated that it arises from solar heating of the detached haze layer, which can also generate waves above the layer. In general, aerosols have a large impact on the energetics and therefore dynamics of the upper atmosphere. This highlights an interesting aspect of the observed light curves. In T41 I and similar occultations the 500 km layer is a stable feature whereas the altitude and amplitude of the higher altitude layer changes slightly between occultations. This makes sense, of course, because we would not expect to observe the density minima and maxima at exactly the same altitude at all times if they are caused by wave motions. We showed earlier that the higher altitude layer arises mostly from perturbations in the density profiles of the minor species whereas aerosol extinction is significant within the detached haze layer. Because the altitude of the detached haze layer does

not oscillate, this indicates that the properties of the wave are modified by haze layers.

We have shown that large perturbations caused by low frequency waves are possible in principle – although this conclusion must be verified by self-consistent simulations and a systematic analysis of the observed density profiles that will be available in the future. Incidentally, such perturbations are routinely observed in the mesosphere on Earth. For instance, the density profiles of O and O₃ indicate that gravity waves in the vicinity of the mesopause can induce larger relative perturbations in the density profiles of the minor species than those implied by the temperature or total density perturbations (e.g., Xu et al., 2000, 2003). These perturbations are mostly associated with short chemical timescales and the resulting large variations in the chemical source terms driven by the temperature and density perturbations while wave advection plays only a minor role. On Titan the chemical time constants of the minor species are generally much longer than on Earth and wave advection is more important. However, we note that the chemical timescales for C₆H₆ and C₄H₂ are comparable to the implied timescale of the wave motions, and for these species chemical perturbations caused by the wave could also be important.

Given that there are some uncertainties related to the properties of the waves, it is prudent to explore other possible explanations for the fluctuations in the density profiles of the minor species. Needless to say, an upward vertical velocity of ~20–30 cm s⁻¹ driven by circulation in a region where the mixing ratios increase with altitude could also produce a sink in the density profiles of the minor species. In this regard it is interesting to note that the density minima around 680 km in the T41 I data coincide rather closely with the density maxima at a similar altitude in the T53 data. Further, the sink near 680 km in the T41 I data can also be interpreted as a local minimum in the mixing ratios of the minor species if the model profiles are properly adjusted (see Fig. 32). Presumably, then, the maxima in the T53 data could be explained by downwelling.

Because fast mesospheric winds are feasible, a vertical velocity of 20–30 cm s⁻¹ is not unreasonable. However, it is not easy to see what type of circulation would cause such localized features in the density profiles. Rather, it is possible that some combination of circulation and gravity waves is responsible for the appearance of the layers. The properties of the wave are somewhat different in the T53 data and this could well be related to differences in the dynamical state of the atmosphere between the two occultations. We note that self-consistent solutions for the perturbation amplitudes of temperature, velocity, and the densities of the different species are required to clarify the influence of the background dynamics on the waves and thus on the composition of the atmosphere (e.g., Xu et al., 2003). The solutions should be pursued along with circulation models that take into account the heating of the haze layers and mechanical forcing by the waves. The results should be coupled with realistic thermal structure calculations that assess the impact of the fluctuations in the density profiles of the aerosols and species such as HCN on the temperature profile. Clearly, these types of calculations are complex and will only be justified once more observations become available to facilitate better comparison between models and data.

We note that abrupt altitude variations in K_{zz} can also cause a minimum in the density profiles if the value of K_{zz} decreases sharply below the production layer, provided that there is another source (chemical or otherwise) of the relevant species at lower altitudes. For instance, Wilson and Atreya (2004) were able to fit the deep minimum in the Voyager/UVS density profile of C₂H₂ (Ver-vack et al., 2004) by adopting a profile for K_{zz} that increases sharply with altitude and reaches values in the thermosphere that imply that the homopause is located near 1000 km. We tested our photochemical calculations by adopting a number of different profiles for

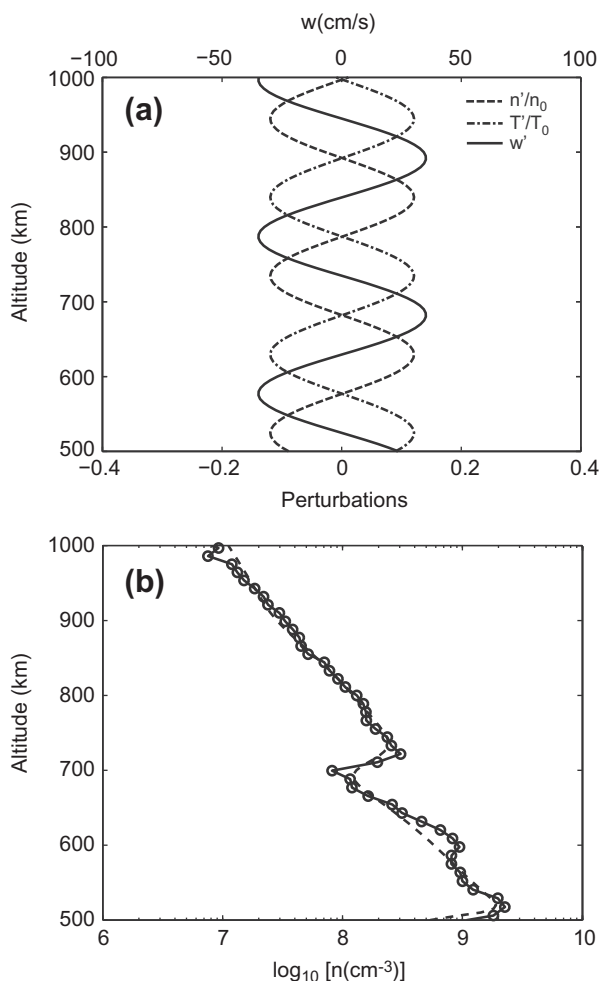


Fig. 34. The density profile of C₂H₂ fitted with the numerical perturbation model. (a) Shows the fixed perturbations to temperature, density and vertical velocity adopted for the simulations and (b) compares the results from the model (dashed line) with the data (circles). We adopted values of $\lambda = 210$ km, $\rho_1/\rho_0 = 0.12$ and $w' = 35$ cm s⁻¹. The key result is that the density perturbation for C₂H₂ is larger than the overall density perturbation between 650 and 700 km because of the large positive gradient in the mixing ratio of C₂H₂ in this region.

K_{zz} but could not find combinations of chemistry and K_{zz} that produce the sharp minima observed in the data. Further, the value of K_{zz} would have to be lower by two orders of magnitude than the values given by Yelle et al. (2008) to prevent mixing from affecting the depth of the density minima in the absence of wave advection.

We also verified that the minima are not caused by condensation of any of the minor species onto, say, meteoritic dust (e.g., Liang et al., 2007). Lavvas et al. (2009) have already shown that condensation of the key constituents is unlikely at the temperatures measured by HASI, particularly in the detached haze layer. However, the CH_4 temperature derived for T41 I is 20–30 K cooler than the HASI temperature between 600 and 750 km and the temperatures derived for T53 are 30–40 K cooler than the HASI profile at similar altitudes. Even so, we calculated saturation densities that are orders of magnitude higher than the observed densities. The only exception is C_6H_6 during T53. The saturation density for C_6H_6 in the temperature minimum of 890 km in the T53 data is 10^3 cm^{-3} . Surprisingly, this implies that C_6H_6 is allowed to condense at this location. Thus condensation of C_6H_6 and similar species can occur periodically in the mesosphere and lower thermosphere.

4.4. High altitude aerosols

Based on the assumption that aerosols are solely responsible for extinction at wavelengths between 1850 and 1900 Å, Liang et al. (2007) argued that they are detectable up to the altitude of 1000 km. This is an important result because, together with INMS and CAPS measurements (Waite et al., 2007; Coates et al., 2007), it implies that the seed particles for aerosols are created in the thermosphere. We agree with Liang et al. (2007) in principle but note that the possible presence of other absorbers may lead to lower aerosol extinction at higher altitudes. The formation of the aerosols may be initiated by the growth of polycyclic aromatic compounds (PACs) (Lavvas et al., 2011, and references therein). These are initially formed by reactions of C_6H_6 with radicals such as C_2H , CN, and HCCN. We point out that reactions involving C_6H_6 and CH_3 could also be important. Although not very reactive, CH_3 is the most abundant hydrocarbon radical in Titan's atmosphere. These reactions could lead to the formation of toluene and xylenes.

The formation and evolution of the aerosols by the PAC mechanism proceeds in three stages at different altitudes in the atmosphere (Lavvas et al., 2011). The PACs are formed at altitudes between ~650 and 1000 km where only a small fraction of them generates the seed particles for aerosol growth. The seed particles coagulate to form larger particles while they also undergo surface growth through the deposition of PACs onto the surface of the seed particles. The surface chemistry allows them to retain a roughly spherical shape above ~650 km. Below 650 km aggregation begins to dominate over surface deposition and the fractal dimension D_f changes from 3 to 2 between 500 and 650 km. In this region aerosol extinction should increase with decreasing altitude. Such an increase is seen below 700 km in the T41 I and the T53 data. Extinction decreases steeply with altitude below the detached haze layer as spherical growth is replaced by fractal aggregate growth that leads to the formation of the fractal aerosols observed in the main haze layer (Tomasko et al., 2008).

As we noted in Section 3.4, the Cassini/ISS images are limited to altitudes below ~600 km and thus we cannot constrain the properties of the high altitude aerosols directly. However, the properties of the aerosols are to some degree constrained by the observed temperature profile and the extinction coefficients shown in Fig. 28. A heating rate of $\sim 2 \times 10^{-9} \text{ erg cm}^{-3} \text{ s}^{-1}$ is required to produce a temperature of 160–170 K near 750 km (Yelle, 1991). The solar flux at Titan, on the other hand, is $\sim 1.5 \times 10^4 \text{ erg cm}^{-2} \text{ s}^{-1}$. Thus an aerosol extinction coefficient of $1.3 \times 10^{-13} \text{ cm}^{-1}$ at 5000 Å implies a heating rate comparable to that due to the gas-

eous opacity in the upper atmosphere. The UV extinction coefficient derived from the T41 I data is $\sim 8 \times 10^{-10} \text{ cm}^{-1}$ at 1875 Å. Unless there is an unaccounted source of cooling in the atmosphere near 750 km, this means that the ratio of the visible (5000 Å) to the UV extinction coefficient that characterizes the high altitude aerosols is less than $\sim 2 \times 10^{-4}$.

We find that small particles (with radii less than ~10 nm) and an imaginary index of refraction $k < 10^{-4}$ at 5000 Å are consistent with this constraint. We note that the required value of k is much smaller than values of k between 0.1 and 0.01 that apply to Khare et al. (1984) tholins or constraints obtained from DISR observations for aerosols at lower altitudes (Lavvas et al., 2010). We also calculated the net heating rates based on refractive indices adjusted to match with DISR observations. The resulting heating rates vary between 2 and $6 \times 10^{-7} \text{ erg cm}^{-3} \text{ s}^{-1}$ for spherical particles with radii ranging from 50 to 5 nm. We note that these calculations include infrared cooling from aerosols, with the refractive index at infrared wavelengths based on CIRS observations (Vinatier et al., 2010b). The net heating rates are two orders of magnitude higher than the heating rate based on gaseous opacity, and thus the optical properties of the high altitude aerosols probably differ from those observed within and below the detached haze layer.

The sedimentation velocity of aerosols with a radius of $r_a = 15 \text{ nm}$ at $z = 750 \text{ km}$ is 58 cm s^{-1} . This means that the sedimentation timescale is faster than the timescales for eddy diffusion and wave advection with $w_1 \sim 30 \text{ cm s}^{-1}$ (see Section 4.3). If we assume that the high altitude enhancement in the T41 I aerosol extinction profile is related to wave motions, we can obtain another loose constrain on the particle size. The sedimentation timescale is comparable to the wave advection timescale for particles with radii of $r_a < 7 \text{ nm}$. It should be noted, though, that the fluctuation in the extinction profile of the high altitude aerosols in the T41 I data is smaller than the relative fluctuations in the density profiles of the minor species. Thus the density of the high altitude aerosols is probably controlled by some intermediate regime between sedimentation and wave effects and slightly larger radii are also allowed.

5. Summary and conclusions

We reanalyzed the Cassini/UVIS stellar occultations obtained during flyby Tb (Shemansky et al., 2005; Liang et al., 2007) in December 2004 and presented new analyses of other occultations that took place between flybys Tb and T58 in July 2009. In particular, we concentrated on two occultations obtained during flyby T41 in February 2008 and T53 in April 2009. These occultations were chosen because of the stability of the spacecraft during the occultations and the high altitude sampling resolution of 0.4–2 km. Because the data were binned in altitude, these occultations allow for a significantly better S/N in the density profiles and transmission spectra when compared with, for instance, the Tb occultations at similar resolution. Thus the T41 and T53 observations represent a good benchmark for identifying different absorbers and retrieving column density profiles. However, we also obtained light curves for all of the other stellar occultations that were recovered from the PDS database.

In addition to confirming the detection of CH_4 , C_2H_2 , C_2H_4 , C_4H_2 , C_2H_6 , and HCN in the data (Shemansky et al., 2005), we identified absorption bands by HC_3N and C_6H_6 . The detection of C_6H_6 is important because radical chemistry involving C_6H_6 may play a role in forming the seed particles for aerosol growth (Lavvas et al., 2011). We also showed that extinction by aerosols increases with decreasing altitude below 700 km (see also, Liang et al., 2007). An increase in the extinction coefficients of the aerosols may be associated with aggregation of the aerosol particles and a gradual

change of the fractal dimension D_f from 3 to 2 (Lavvas et al., 2011). We note that aerosol extinction above ~ 700 km is uncertain because the presence of additional absorbers such as C_6H_2 cannot be ruled out.

We derived density profiles for the minor species identified in the data and the extinction profiles for the aerosols. In order to obtain these density profiles, we used the most recently measured absorption cross sections (Table 2). Where possible, we used cross sections measured at temperatures comparable to those observed in the upper atmosphere of Titan. The extinction cross sections for the aerosols were derived from Mie theory based on the optical properties of the Khare et al. (1984) tholins. We obtained column density profiles for different absorbers by fitting the transmission spectra at a predetermined altitude resolution that varied between 1 and 8 km. The best fit is based on a forward model that takes into account the wavelength resolution of the UVIS instrument and atmospheric transmission. We used the Levenberg–Marquardt algorithm to obtain the most likely combination of column densities at each impact parameter that gives rise to the observed extinction. By analyzing synthetic data based on number density profiles obtained from a photochemical model, we demonstrated that this method is reliable in separating the contributions of different absorbers from each other.

The column density profiles were converted into number density profiles by a controlled inversion that relies on the Tikhonov regularization technique (Tikhonov and Arsenin, 1977). This method yields the most likely number density profiles that give rise to the observed column density profiles and their uncertainties. The combination of the LM retrieval of the column density profiles and the inversion by Tikhonov regularization has been used before in the analysis of stellar occultations on Mars (Quemerai et al., 2006) and Earth (e.g., Kyrola et al., 2010). We also tested this method by analyzing synthetic occultations and found that it can be used to derive reliable number density profiles – even when these profiles contain large perturbations. The density profiles were retrieved between ~ 600 and 1200 km for CH_4 , between ~ 400 and 1000 km for C_2H_2 , C_2H_4 and C_4H_2 , between ~ 550 and 1000 km for HCN and HC_3N , and between ~ 400 and 900 km for C_6H_6 . The extinction coefficients for the aerosols were derived for altitudes between 400 and 900 km. In general, the resulting number density profiles have an altitude resolution of 10–50 km.

Together with Cassini/CIRS and Cassini/INMS measurements, our results confirm that hydrocarbon and nitrile species are formed in the thermosphere and that their mixing ratios increase with altitude below 800 km. This behavior is in line with predictions by photochemical models. We also compared our results with previously retrieved density profiles between 500 and 1200 km. Our results differ from those of Vervack et al. (2004) based on Voyager/UVS observations for species other than CH_4 . The T41 I density profile of CH_4 agrees well with the UVS measurements. It also agrees well with the density profile of CH_4 retrieved by Shemansky et al. (2005) from the UVIS Tb data at altitudes below 1200 km. We note that there are large variations in the density profiles between the T41 I and T53 observations. Thus some of the discrepancies between the UVS and UVIS data could be due to variability in the atmosphere. This is unlikely to be the case for C_2H_2 though. Both our analysis and the work of Shemansky et al. (2005) indicate that the UVS densities of C_2H_2 are systematically underestimated between 550 and 850 km.

The light curves based on the occultations observed between December 2004 and July 2009 contain distinct extinction layers. The appearance of these layers changes with time and location, but overall they are stable features that vary only slowly over time. In particular, we identified two distinct layers: a low altitude layer between 450 and 550 km and a high altitude layer that appears either as a broad extinction layer centered around 600 km or as a

sharp layer between 700 and 800 km. The low altitude extinction layer coincides with the detached haze layer (Porco et al., 2005). We determined the altitude of this layer as a function of time based on the UVIS data and showed it to be consistent with the rapid change in altitude from ~ 500 km to 450 km that was observed in recent Cassini/ISS images (West et al., 2011). We note that this collapse, and the accompanying changes in the atmospheric structure, may be responsible for some of the differences in the density and temperature profiles between the T41 and T53 data. A comprehensive study of the existing occultations should verify whether this is the case or not.

The high altitude extinction layer is mostly due to large perturbations in the density profiles of the gaseous absorbers. Such perturbations also coincide with the detached haze layer. The temperature profiles derived from the T41 I and T53 density profiles of CH_4 also contain perturbations. These perturbations are similar to the waves observed in the HASI data (Fulchignoni et al., 2005) in that they have a vertical wavelength of ~ 100 –200 km and an amplitude of 10–20 K. We derived temperature gradients based on the CH_4 profiles and found that the wave can drive local convective instabilities near the minima of the temperature profile. Such behavior is consistent with breaking gravity waves driven by tides that were proposed as an explanation for the HASI observations by Strobel (2006).

The relative perturbations in the density profiles of the minor species other than CH_4 are significantly larger than the relative temperature perturbations. We demonstrated that a low frequency wave, such as a tidal wave, can cause substantially larger relative density perturbations than the relative temperature perturbations for minor species whose mixing ratio increases steeply with altitude. We showed that the large perturbations in the density profiles of C_2H_2 , C_2H_4 , C_4H_2 , C_6H_6 , HCN and HC_3N can be approximately fitted by a wave that has a vertical wavelength of ~ 200 km and a frequency based on the diurnal time constant. Thus our results provide evidence for large-scale, low-frequency waves that affect the temperature and density profiles in Titan's mesosphere and lower thermosphere – although the observed perturbations probably represent a superposition of several waves. It is interesting to note that similar perturbations were observed in the density profiles of HCN and HC_3N at high northern latitudes in the stratosphere by Teanby et al. (2007). It has been suggested that these perturbations are associated with waves and global dynamics in and near the polar vortex (Teanby et al., 2009). We note that waves can also influence the density profiles directly, and not only through their effect on global dynamics.

We note that gravity waves cause large perturbations in the mixing ratios of the minor species in the mesosphere on Earth (e.g., Xu et al., 2000, 2003; Xu and Smith, 2004). On Earth, the large perturbations near the mesopause arise mostly from perturbations in the chemical reaction rates that are driven by waves. On Titan, the photochemical timescales are long and wave advection is likely to be more important. The potential similarities in the dynamics of the mesosphere between Titan and the Earth implied by our results are interesting. On Earth the density profiles of the minor species and mesospheric circulation are both shaped by gravity waves and the same may be true on Titan. However, this needs to be verified by a careful analysis of more data that is interpreted with the aid of circulation and thermal structure models that account for the heating of the haze layers and momentum and energy transfer by waves.

We obtained the extinction coefficients of the aerosols as a function of altitude assuming that the aerosols are spherical tholins. As we noted above, aerosol extinction increases with decreasing altitude below 700 km. This could be consistent with a production region between 700 and 1000 km and a transition from spherical growth to aggregation between 500 and 700 km (Lavvas et al., 2011). The extinction coefficients contain a sharp peak that coincides with

the detached haze layer and another broader peak associated with the high altitude extinction layers. By comparing the UVIS extinction coefficients (Liang et al., 2007) with ISS images, Lavvas et al. (2009) showed that the radius of the aerosols in the detached haze layer is $r_a \sim 40$ nm. Unfortunately, the UVIS extinction data alone cannot be used to obtain firm constraints on the size of the high altitude aerosols. Assuming that the wavelength dependency of the aerosol cross sections is proportional to $\lambda^{-\alpha}$, the data are consistent with $\alpha < 2.5$ at all altitudes. This range of α includes all reasonable particle sizes. However, we used the temperature profile in the T41 I data to obtain a loose upper limit of $r_a \sim 10$ nm at 700 km for the radius of the aerosols. If correct, this means that the particles grow significantly between 500 and 700 km.

We have taken the first steps in characterizing the density and temperature profiles in Titan's mesosphere and lower thermosphere – a region of the atmosphere that has received little attention to date because it falls between the thermosphere above and the stratosphere below and is thus out of reach by most Cassini instruments. We hope that our work conveys the remarkable richness of information available in the UVIS stellar occultation data about this fascinating region of Titan's atmosphere that holds the key to the formation of organic hazes that have held the interest of the scientific community for decades.

Acknowledgments

We thank B. Semonov for extensive advice on using the SPICE routines and libraries to calculate the occultation geometry. We thank Greg Holsclaw and William McClintock for communications regarding the properties of the Cassini/UVIS instrument. We also thank D. Strobel, P. Rannou and I. Muller-Wodarg for particularly fruitful conversations, and R. Vervack for providing the Voyager/UVS results in a convenient form. We thank the UVIS team for inspiration and for making this work possible. This research was supported by NASA's Cassini Data Analysis Program through Grant NNX09AD14G and Planetary Atmospheres Program through Grant NNX09AB58G.

Appendix A. Linear perturbation approximation for waves in the density profiles of minor species

Here we treat the different minor species as passive tracers of the wave motions. This implies that the timescale of the wave motion is much faster than the chemical lifetime of the tracers and that the perturbations in the mixing ratios of the minor species do not affect the overall properties of the wave. Our purpose is simply to examine the impact of different types of (gravity) waves on the density profiles of the trace gases. Consider the equation of continuity for a minor species s given by:

$$\frac{\partial q_s}{\partial t} + w \frac{\partial q_s}{\partial r} + \frac{v}{r} \frac{\partial q_s}{\partial \theta} + \frac{u}{r \sin \theta} \frac{\partial q_s}{\partial \phi} = \frac{1}{r^2 \rho} \frac{\partial}{\partial r} \left[r^2 \rho (K_{zz} + D_s) \frac{\partial q_s}{\partial r} - r^2 \rho D_s \left(1 - \frac{M_s}{M} - \frac{H}{M} \frac{\partial M}{\partial r} \right) \frac{q_s}{H} \right] \quad (\text{A.1})$$

where q_s is the mass mixing ratio, D_s is the average molecular diffusion coefficient, M is the mean molecular weight, and H is the pressure scale height. We assume that the waves propagate in zonal and vertical directions only and expand this equation by using perturbed quantities of the form $f(t, r, \phi) = f_0(t, r) + f'(t, r, \phi)$. Note that the mean state $f_0(t, r)$, which is characterized by an equation similar to the equation of continuity above, does not vary with latitude or longitude and that the perturbations are considered small. The latter condition implies that the products of perturbations are negligible. Further, we assume that the mean molecular weight and D_s are constant with altitude, and that K_{zz} , M , and D_s are not

perturbed. We also assume that terms including the ratio ρ'/ρ_0 and terms containing the gradient of the mean or perturbed scale height divided by the mean scale height are negligible. With these assumptions we obtain:

$$\begin{aligned} \frac{\partial q'_s}{\partial t} + w_0 \frac{\partial q'_s}{\partial r} + w' \frac{\partial q_{s0}}{\partial r} + \frac{u_0}{r \sin \theta} \frac{\partial q'_s}{\partial \phi} \\ = K_s \frac{\partial^2 q'_s}{\partial r^2} + \frac{\partial q'_s}{\partial r} \left(\frac{2K_s}{r} - \frac{K_s}{H_\rho} + \frac{\partial K_s}{\partial r} - \frac{D_s \mu_s}{H} \right) \\ + q'_s \left(\frac{D_s \mu_s}{H H_\rho} - \frac{2D_s \mu_s}{r H} \right) + \frac{\partial \rho'}{\partial r} \left(\frac{K_s}{\rho_0} \frac{\partial q_{s0}}{\partial r} - \frac{D_s \mu_s}{\rho_0 H} q_{s0} \right) \end{aligned} \quad (\text{A.2})$$

where

$$\begin{aligned} K_s &= K_{zz} + D_s \\ \mu_s &= \left(1 - \frac{M_s}{M} \right) \\ H_\rho &= -\frac{1}{\rho_0} \frac{\partial \rho_0}{\partial r} \end{aligned}$$

Generally we will assume that $H_\rho \approx H$. We scaled the terms in Eq. (A.2) with characteristic values for Titan's atmosphere at altitudes between 500 and 1000 km. In this region we assumed that $K_s \approx 10^7 \text{ cm}^2 \text{ s}^{-1}$, $H \approx 60$ km, and $D_s \approx 10^7 \text{ cm}^2 \text{ s}^{-1}$ (near the homopause). The scaling analysis allows us to simplify the equation by excluding terms that include the ratio $2/r$.

We assume that the perturbations are waves with a constant amplitude with respect to altitude. This is not a valid assumption for atmospheric gravity waves in general, but it is reasonable for local analysis or regions where the waves have become saturated so that their amplitude no longer grows with altitude. Thus the perturbations are expressed as:

$$\begin{aligned} q'_s &= q_{s1} \exp[i(mr + k\phi - \omega t + \theta_q)] \\ w' &= w_1 \exp[i(mr + k\phi - \omega t + \theta_w)] \\ \rho' &= \rho_1 \exp[i(mr + k\phi - \omega t + \theta_\rho)] \end{aligned}$$

where m and k are the vertical and zonal wavenumbers, and θ_w , θ_ρ , and θ_q are the phase angles of w' and ρ' and q'_s , respectively. Because we consider the impact of generic waves on the density profiles of the minor species and do not calculate ρ' and w' self-consistently, we have not derived formal polarization equations to specify the phase angles. Instead, we assume simply that $\theta_w = \theta_\rho + \pi/2$. Substituting these perturbations into Eq. (A.2) yields:

$$\begin{aligned} q'_s \left[\frac{\Omega}{m} - w_0 - \frac{K_s}{H} + \frac{\partial K_s}{\partial r} - \frac{D_s \mu_s}{H} + i \left(m K_s - \frac{i D_s \mu_s}{m H^2} \right) \right] \\ = -\frac{\partial q_{s0}}{\partial r} \left(\frac{i w'}{m} + \frac{\rho'}{\rho_0} K_s \right) + \frac{D_s \mu_s}{H} \frac{\rho'}{\rho_0} q_{s0} \end{aligned} \quad (\text{A.3})$$

where $\Omega = \omega - k u_0 / (r \sin \theta)$ is the intrinsic Doppler-shifted wave frequency, which can also be expressed in terms of the zonal phase speed as $\Omega = k_\phi (c_\phi - u_0)$ with $k_\phi = k / (r \sin \theta)$. As an example, we consider waves whose phase propagates eastward towards lower altitudes (e.g., Strobel, 2006) well below the homopause so that $k > 0$, $m < 0$, and $K_{zz} \gg D_s$. Further, we assume that K_{zz} is approximately constant with altitude. Canceling $\exp[i(mr + k\phi - \omega t)]$ and some algebra then yields:

$$r_{s1} \exp(i\theta_q) = \frac{1}{q_{s0}} \frac{\partial q_{s0}}{\partial r} \frac{[(w_1/m) + (\rho_1/\rho_0)K_{zz}] \exp(i\theta)}{\sqrt{[c_{r1} - w_0 - (K_{zz}/H_0)]^2 + m^2 K_{zz}^2}} \quad (\text{A.4})$$

$$\theta = \theta_\rho + \pi - \tan^{-1} \left[\frac{m K_{zz}}{c_{r1} - w_0 - (K_{zz}/H_0)} \right] \quad (\text{A.5})$$

where $r_{s1} = q_{s1}/q_{s0}$ and $c_{r1} = \Omega/m$ is the intrinsic vertical phase speed. Here we do not specify the type of mixing that is parameterized by

K_{zz} , other than that it is diffusive in nature. However, we acknowledge that this mixing could arise partly from the waves themselves through their effect on the mean mixing ratio q_{s0} .

Next we consider the advection limit where K_s and $D_s \rightarrow 0$ in Eq. (A.3). In this case we have:

$$q'_s = -\frac{iw'}{m} \left(\frac{\Omega}{m} - w_0 \right)^{-1} \frac{\partial q_{s0}}{\partial r} \quad (\text{A.6})$$

Assuming that the waves propagate vertically only and that there is no background flow, this equation becomes:

$$q'_s = -\text{sgn}(m) \frac{iw'}{\omega} \frac{\partial q_{s0}}{\partial r} \quad (\text{A.7})$$

We note that this equation agrees with Eq. (7) of Xu and Smith (2004). For downward propagating phase ($m < 0$) with $\theta_w = \theta_\rho + \pi/2$, it implies that the perturbations in the mixing ratios are in phase with the temperature perturbations when q_{s0} increases with altitude.

References

- Ajello, J.M. et al., 2007. Titan airglow spectra from the Cassini Ultraviolet Imaging Spectrograph (UVIS): EUV analysis. *Geophys. Res. Lett.* 34, L24204.
- Ajello, J.M. et al., 2008. Titan airglow spectra from the Cassini Ultraviolet Imaging Spectrograph: FUV disk analysis. *Geophys. Res. Lett.* 35, L06102.
- Broadfoot, A.L. et al., 1981. Extreme ultraviolet observations from Voyager 1 encounter with Saturn. *Science* 212, 206–211.
- Capalbo, F.J., 2010. Titan's Atmospheric Composition from Cassini Ultraviolet Imaging Spectrograph Data Analysis. Master's Thesis. Luleå University of Technology, Kiruna, Sweden. ISSN:1653-0187 – ISRN: LTU-PB-EX-10/058-SE.
- Chen, F.Z., Wu, R.C.Y., 2004. Temperature-dependent photoabsorption cross sections in the VUV–UV region. I. Methane and ethane. *J. Quant. Spectrosc. Radiat. Transfer* 85, 195–209.
- Coates, A.J. et al., 2007. Discovery of heavy negative ions in Titan's ionosphere. *Geophys. Res. Lett.* 34, L22103.
- Coustenis, A. et al., 2010. Titan trace gaseous composition from CIRS at the end of the Cassini–Huygens prime mission. *Icarus* 207, 461–476.
- Cui, J., Yelle, R.V., Volk, K., 2008. Distribution and escape of molecular hydrogen in Titan's thermosphere and exosphere. *Geophys. Res. Lett.* 113, E10004.
- Cui, J. et al., 2009. Analysis of Titan's neutral upper atmosphere from Cassini Ion Neutral Mass Spectrometer measurements. *Icarus* 200, 581–615.
- Esposito, L.W. et al., 2004. The Cassini ultraviolet imaging spectrograph investigation. *Space Sci. Rev.* 115, 299–361.
- Fahr, A., Nayak, A.K., 1994. Temperature dependent ultraviolet absorption cross sections of 1,3 butadiene and butadiyne. *J. Chem. Phys.* 101, 725–731.
- Ferradaz, T. et al., 2009. Temperature-dependent photoabsorption cross-sections of cyanoacetylene and diacetylene in the mid- and vacuum-UV: Application to Titan's atmosphere. *Planet. Space Sci.* 57, 10–22.
- Flasar, F.M. et al., 2005. Titan's atmospheric temperatures, winds, and composition. *Science* 308, 975–978.
- Friedson, A.J., 1994. Gravity waves in Titan's atmosphere. *Icarus* 109, 40–57.
- Fulchignoni, M. et al., 2005. In situ measurements of the physical characteristics of Titan's environment. *Nature* 438, 785–791.
- Hinson, D.P., Tyler, G.L., 1983. Internal gravity waves in Titan's atmosphere observed by Voyager radio occultations. *Icarus* 54, 337–352.
- Jacobson, M.Z., 1999. *Fundamentals of Atmospheric Modeling*. Cambridge University Press, Cambridge, UK.
- Khare, B.N. et al., 1984. Optical constants of organic tholins produced in a simulated Titanian atmosphere: From soft X-ray to microwave frequencies. *Icarus* 60, 127–137.
- Kyrola, E., Sihvola, E., Kotivuori, Y., Tikka, M., Tuomi, T., 1993. Inverse theory for occultation measurements. I. Spectral inversion. *J. Geophys. Res.* 98, 7367–7381.
- Kyrola, E. et al., 2010. Retrieval of atmospheric parameters from GOMOS data. *Atmos. Chem. Phys. Discuss.* 10, 10145–10217.
- Lavvas, P., Coustenis, A., Vardavas, I.M., 2008a. Coupling photochemistry with haze formation in Titan's atmosphere. Part I: Model description. *Planet. Space Sci.* 56, 27–66.
- Lavvas, P., Coustenis, A., Vardavas, I.M., 2008b. Coupling photochemistry with haze formation in Titan's atmosphere. Part II: Results and validation with Cassini/Huygens data. *Planet. Space Sci.* 56, 67–99.
- Lavvas, P., Yelle, R.V., Vuitton, V., 2009. The detached haze layer in Titan's mesosphere. *Icarus* 201, 626–633.
- Lavvas, P., Yelle, R.V., Griffith, C.A., 2010. Titan's vertical aerosol structure at the Huygens landing site: Constraints on particle size, density, charge, and refractive index. *Icarus* 210, 832–842.
- Lavvas, P., Sander, M., Kraft, M., Imanaka, H., 2011. Surface chemistry and particle shape: Processes for the evolution of aerosols in Titan's atmosphere. *Astrophys. J.* 728, 80–91.
- Lee, A.Y.T. et al., 2001. Enhancement of deuterated ethane on Jupiter. *Astrophys. J. Lett.* 551, L93–L96.
- Liang, M.-C., Yung, Y.L., Shemansky, D.E., 2007. Photolytically generated aerosols in the mesosphere and thermosphere of Titan. *Astrophys. J. Lett.* 661, L199–L202.
- McClintock, W.E., Lawrence, G.M., Kohnert, R.A., Esposito, L.W., 1993. Optical design of the ultraviolet imaging spectrograph for the Cassini mission to Saturn. *Opt. Eng.* 32, 3038–3046.
- Moreno, R., Marten, A., Hidayat, T., 2005. Interferometric measurements of zonal winds on Titan. *Astron. Astrophys.* 437, 319–328.
- Muller-Wodarg, I.C.F., Yelle, R.V., Mendillo, M.J., Aylward, A.D., 2003. On the global distribution of neutral gases in Titan's upper atmosphere and its effect on the thermal structure. *J. Geophys. Res.* 108, A121453.
- Muller-Wodarg, I.C.F., Yelle, R.V., Borggren, N., Waite Jr., J.H., 2006. Waves and horizontal structures in Titan's thermosphere. *J. Geophys. Res.* 111, A12315.
- Porco, C. et al., 2005. Imaging of Titan from the Cassini spacecraft. *Nature* 434, 159–168.
- Quemerais, E. et al., 2006. Stellar occultations observed by SPICAM on Mars Express. *J. Geophys. Res.* 111, E09S04.
- Rodgers, C.D., 2000. *Inverse Methods for Atmospheric Sounding: Theory and Practice*. World Scientific Publishing Co. Pte. Ltd., Singapore.
- Shemansky, D.E. et al., 2005. The Cassini UVIS stellar probe of the Titan atmosphere. *Science* 308, 978–982.
- Sicardy, B. et al., 1999. The structure of Titan's stratosphere from the 28 Sgr occultation. *Icarus* 142, 357–390.
- Smith, G.R. et al., 1982. Titan's upper atmosphere: Composition and temperature from the EUV solar occultation results. *J. Geophys. Res.* 87, 1351–1359.
- Stevens, M.H. et al., 2011. The production of Titan's ultraviolet nitrogen airglow. *J. Geophys. Res.* 116, A05304.
- Strobel, D.F., 2006. Gravitational tidal waves in Titan's upper atmosphere. *Icarus* 182, 251–258.
- Strobel, D.F., Summers, M.E., Zhu, X., 1992. Titan's upper atmosphere: Structure and ultraviolet emissions. *Icarus* 100, 512–526.
- Suto, M., Wang, J.S., Shan, J., Lee, L.C., 1992. Quantitative photoabsorption and fluorescence spectroscopy of benzene, naphthalene, and some derivatives at 106–295 nm. *J. Quant. Spectrosc. Radiat. Transfer* 48, 79–89.
- Teanby, N.A. et al., 2007. Vertical profiles of HCN, HC₃N, and C₂H₂ in Titan's atmosphere derived from Cassini/CIRS data. *Icarus* 186, 364–384.
- Teanby, N.A., de Kok, R., Irwin, P.G.J., 2009. Small-scale composition and haze layering in Titan's polar vortex. *Icarus* 204, 645–657.
- Tikhonov, A.N., Arsenin, V.Y., 1977. *Solutions of Ill-Posed Problems*. V.H. Winston & Sons, a Division of Scripta Technica, Inc., Washington, DC, USA.
- Tomasko, M.G. et al., 2008. A model of Titan's aerosols based on measurements made inside the atmosphere. *Planet. Space Sci.* 56, 669–707.
- Vervack, R.J., Sandel, B.R., Strobel, D.F., 2004. New perspectives on Titan's upper atmosphere from a reanalysis of the Voyager 1 UVS solar occultations. *Icarus* 170, 91–112.
- Vinatier, S. et al., 2010a. Analysis of Cassini/CIRS limb spectra of Titan acquired during the nominal mission. I. Hydrocarbons, nitriles, and CO₂ vertical mixing ratio profiles. *Icarus* 205, 559–570.
- Vinatier, S. et al., 2010b. Analysis of Cassini/CIRS limb spectra of Titan acquired during the nominal mission. II. Aerosol extinction profiles in the 600–1420 cm⁻¹ spectral range. *Icarus* 210, 852–866.
- Vuitton, V., Yelle, R.V., McEwan, M.J., 2007. Ion chemistry and N-containing molecules in Titan's upper atmosphere. *Icarus* 191, 722–742.
- Vuitton, V., Yelle, R.V., Cui, J., 2008. Formation and distribution of benzene on Titan. *J. Geophys. Res.* 113, E05007.
- Vuitton, V., Yelle, R.V., Lavvas, P., 2009. Composition and chemistry of Titan's thermosphere and ionosphere. *Philos. Trans. R. Soc. A* 367, 729–741.
- Waite Jr., J.H. et al., 2005. Ion neutral mass spectrometer results from the first flyby of Titan. *Science* 308, 982–986.
- Waite Jr., J.H. et al., 2007. The process of tholin formation in Titan's upper atmosphere. *Science* 316, 870–875.
- West, R.A. et al., 2011. The evolution of Titan's detached haze layer near the equinox. *J. Geophys. Res.* 38, L06204.
- Wilson, E.H., Atreya, S.K., 2004. Current state of modeling the photochemistry of Titan's mutually dependent atmosphere and ionosphere. *J. Geophys. Res.* 109, E06002.
- Wu, R.C.Y., Chen, F.Z., Judge, D.L., 2001. Measurements of temperature-dependent absorption cross sections of C₂H₂ in the VUV–UV region. *J. Geophys. Res.* 106, E47629.
- Wu, R.C.Y., Chen, F.Z., Judge, D.L., 2004. Temperature-dependent absorption cross sections in the VUV–UV region: Ethylene. *J. Geophys. Res.* 109, E07S15.
- Xu, J., Smith, A.K., 2004. Studies of gravity wave-induced fluctuations of the sodium layer using linear and nonlinear models. *J. Geophys. Res.* 109, D02306.
- Xu, J., Smith, A.K., Brasseur, G.P., 2000. The effects of gravity waves on distributions of chemically active constituents in the mesopause region. *J. Geophys. Res.* 105, D2126593.
- Xu, J., Smith, A.K., Ma, R., 2003. A numerical study of the effect of gravity-wave propagation on minor species distributions in the mesopause region. *J. Geophys. Res.* 108, D34119.
- Yelle, R.V., 1991. Non-LTE models of Titan's upper atmosphere. *Astrophys. J.* 383, 380–400.
- Yelle, R.V., Cui, J., Muller-Wodarg, I.C.F., 2008. Methane escape from Titan's atmosphere. *J. Geophys. Res.* 113, E10003.
- Yung, Y.L., Allen, M., Pinto, J.P., 1984. Photochemistry of the atmosphere of Titan: Comparison between model and observations. *Astrophys. J. Suppl.* 55, 465–506.